2009-01-0722

# Integration of a Continuous Multi-Component Fuel Evaporation Model with an Improved G-Equation Combustion and Detailed Chemical Kinetics Model with Application to GDI Engines

**Shiyou Yang and Rolf D. Reitz**
University of Wisconsin-Madison



## ABSTRACT

A continuous multi-component fuel evaporation model has been integrated with an improved G-equation combustion and detailed chemical kinetics model. The integrated code has been successfully used to simulate a gasoline direct injection engine. In the multi-component fuel model, the theory of continuous thermodynamics is used to model the properties and composition of multi-component fuels such as gasoline. In the improved G-equation combustion model a flamelet approach based on the G-equation is used that considers multi-component fuel effects. To precisely calculate the local and instantaneous residual which has a great effect on the laminar flame speed, a "transport equation residual" model is used. A Damkohler number criterion is used to determine the combustion mode in flame containing cells. To consider the change of local fuel vapor mixture composition, a "PRF adaptive" method is proposed that formulates a relationship between the fuel vapor mixture PRF number (or Octane number) and the fuel vapor mixture composition based on the mean molecular weight and variance of the fuel vapor mixture composition in each cell. The laminar flame speed has been updated to consider multi-component fuel effects, as a function of pressure, temperature, equivalence ratio, residual, and fuel vapor mixture PRF number. To model the chemistry process in the unburned region in front of the flame and in burned regions behind the flame, a recently developed PRF mechanism is used to describe the multi-component fuel mixture. Simulations of the vaporization of a single droplet with a single-component fuel (iso-octane) are compared with multi-component fuel cases. The vaporization of a spray of multi-component fuel injected into a chamber is simulated for both normal and flash-boiling conditions. The new PRF mechanism is validated against shock tube data. In addition, gasoline direct injection engine combustion is simulated at different manifold absolute pressures, different end-of-fuel injection timings, and different spark ignition timings. The simulated in-cylinder pressures and heat release rates are compared with experiment data and good agreements are found.

## INTRODUCTION

Vaporization of droplets and sprays has been an issue of much interest for decades because of its significance in engineering applications. For simplicity, fuels have been represented as a single-component fuel in most multi-dimensional models, such as the KIVA code [1-5]. However, single-component fuel models are not able to predict the complex behavior of the vaporization of multi-component fuels such as gasoline and diesel. The preferential vaporization of light-end components in multi-component fuels affects greatly the fuel distribution near the spray and can not be represented by single-component models [6]. Studies have been performed on the vaporization of multi-component fuels [6-11].

Multi-component fuel models are classified into two types, i.e. discrete multi-component (DMC) models and continuous multi-component (CMC) models. The discrete component approach has high computational overhead when it is used for fuels with a large number of components, because additional transport equations are to be solved for each species in order to track the fuel composition and the vaporization behavior. The continuous multi-component (CMC) model, which is based on the continuous thermodynamics method [8],

The Engineering Meetings Board has approved this paper for publication. It has successfully completed SAE's peer review process under the supervision of the session organizer. This process requires a minimum of three (3) reviews by industry experts.

ISSN 0148-7191

**SAE Customer Service:** Tel: 877-606-7323 (inside USA and Canada)
Tel: 724-776-4970 (outside USA)
Fax: 724-776-0790
Email: CustomerService@sae.org
**SAE Web Address:** http://www.sae.org

**Printed in USA**

*9-2009-01-0722*

SAE International™

represents the fuel composition as a continuous distribution function with respect to an appropriate parameter such as molecular weight. This enables a reduction of computational load without degrading the predictability of the complex behavior of the vaporization of multi-component fuels [6]. The continuous multi-component (CMC) model was first implemented into the engine simulation KIVA code to simulate multi-component fuel spray and evaporation by Lippert and Reitz [6,9].

For realistic predictions of the vaporization of multi-component fuels in typical engine operating conditions, both normal and boiling evaporation modes must be considered and a smooth change between these two modes is desirable. For this purpose, based on the work of Lippert and Reitz [6,9] Ra and Reitz [12] improved the continuous multi-component (CMC) KIVA code for better predicting multi-component fuel spray and evaporation under a wide range of engine operating conditions. In order to avoid over-prediction or under-prediction of the evaporation mass flux depending on the ambient temperature conditions, Ra and Reitz [12] added a sub-model into the continuous multi-component (CMC) KIVA code in which the droplet surface temperature (which is not necessarily equal to the droplet average temperature) could be separately calculated. However, in the work of Refs. [6-12], only the effects of multi-component fuels on spray and evaporation were considered. In the combustion model the fuel was still considered as a single-component fuel. For engine simulation combustion and pollutant emissions formation are of special concern to most engine researchers. So the effects of multi-component fuels on the combustion process, flame propagation, laminar flame speed, and the effect of different fuel components on chemistry should also be considered.

Understanding the in-cylinder ignition and combustion processes is one of the key factors for successful modeling. The turbulent ignition and combustion process in Spark Ignition (SI) engines is a complicated aero-thermo-chemical process, especially due to the turbulence and chemistry interactions that occur on tremendously different time-scale and length-scale levels [13,14]. To better model the ignition process, a Discrete Particle Ignition Kernel model (DPIK), in which the flame kernel position is marked by particles, was proposed by Fan and Reitz [15]. The level set method (G-equation) is a powerful tool to model both premixed and partially premixed combustion occurring in SI engines. With its application to combustion, Williams [16] first suggested use of a transport equation for a non-reactive scalar, G, for laminar flame propagation. Peters [14,17] subsequently extended this approach to the turbulent flame regime. The turbulent G-equation concept has been successfully applied to SI engine combustion simulations by Dekena et al. [18], Tan [19], and Ewald et al. [20].

To better understand the fundamental engine combustion process and to further improve the versatility of multidimensional models, attention is being given to models incorporating comprehensive elementary chemical kinetics mechanisms. A large amount of work has been done on developing detailed chemical kinetics mechanisms for fuel oxidation and pollutant formation [21]. Further, research on mechanism reduction and parallel computing techniques has made it computationally affordable to incorporate these reduced detailed chemical kinetics mechanisms into multidimensional engine simulations. Liang [22,23,24] successfully incorporated detailed chemical kinetics into the G-equation-based turbulent combustion model, which was implemented into the KIVA-3V release2 code by Tan et al. [25,26]. Specifically, for SI engine combustion, detailed fuel oxidation mechanisms coupled with a reduced $NO_X$ mechanism are applied behind the mean flame front for modeling post flame combustion and $NO_X$ formation. The chemical kinetics mechanisms are also applied in front of the flame front for predicting compression auto-ignition of the end-gas (knock). Also in Liang's work, in the course of coupling detailed chemistry with the G-equation combustion model for the primary heat release calculation within the flame front, the laminar and turbulent flame speed correlations were improved for a better description of the turbulent flame propagation process. In the G-equation-based turbulent combustion model the laminar flame speed is very important for determining the propagation of the flame front (G=0) surface. Also, the local and instantaneous residual value has a great effect on the evaluation of the laminar flame speed. For the calculation of the residual value, Yang et al. [27] used several different empirical methods. In Yang's work [27], several improvements to the G-equation sub-models were proposed, including the precise calculation of "primary heat release" based on the sub-grid scale unburned/burnt volumes of flame-containing cells. Yang et al. [28] also proposed a transport equation residual model incorporating a Damkohler criterion for accurately calculating the local and instantaneous residual in each cell and fundamentally describing the combustion process in the flame-containing cells. However, in the work of Refs. [15,19,22-28], the fuel was only considered as a single-component fuel.

In this paper, we integrate the continuous multi-component (CMC) fuel evaporation model with the improved G-equation combustion and detailed chemical kinetics model. In the integration, to consider the change of local fuel vapor mixture composition, we present a "PRF adaptive" method that formulates a relationship between the fuel vapor mixture PRF number (or Octane number) and the fuel vapor mixture composition based on the mean molecular weight and variance of the fuel vapor mixture composition in each cell. The laminar flame speed is updated to consider the multi-component fuel effects. To model the chemistry process in the unburned region in front of the flame and in burned regions behind the flame, a recently developed PRF mechanism is used to describe the multi-component fuel mixture. To validate the continuous multi-component (CMC) fuel model, simulations of the vaporization of a

single droplet with a single-component fuel, a single droplet with a multi-component fuel, and a spray of a multi-component fuel is studied. The new PRF mechanism is validated against shock tube data. Finally, gasoline direct injection engine combustion simulations at different manifold absolute pressures, different end-of-fuel injection timings, and different spark ignition timings are performed and compared with experiment data.

## MODEL DESCRIPTION

### CONTINUOUS MULTI-COMPONENT (CMC) FUEL MODEL

Suppose a fuel mixture is composed of a large number of components. Assuming that each component species in the fuel mixture can be characterized by the value of one variable, $I$, which represents a macroscopic property, the amount of substance can be expressed via a distribution function, $f(I)$

$$n(I_1, I_2) = \int_{I_1}^{I_2} f(I)dI \tag{1}$$

where $f(I)$ is also called the probability density function (PDF), and $n(I_1, I_2)$ is the amount (without loss of generality suppose it is the mass fraction. While mathematically it is the probability) of the substance with property $I$, such that $I_1 < I < I_2$. $dn = f(I)dI$ is the probability in the differential interval $dI$. The distribution function $f(I)$ has the property that

$$\int_0^\infty f(I)dI = 1 \tag{2}$$

In this paper the independent variable $I$ is chosen to be the species molecular weight. The functional form of the distribution function $f(I)$ is limited to an analytical form, either a Gaussian distribution or a $\Gamma$ (Gamma) distribution, which will be shown later. Now consider a spherical liquid droplet with a large number of components vaporizing in a gaseous environment. The governing equations for the vapor phase fuel, the liquid phase fuel, along with the liquid-vapor equilibrium at the interface between the droplet and surrounding gas, are considered next.

#### Vapor phase transport equations

Based on the continuous thermodynamics approach, the governing equations for the various moments of the fuel vapor distribution in the gas phase can be derived. For the two-parameter-type $\Gamma$ distribution function used in this paper, three equations suffice for the calculations. The governing equations for the continuity, mean molecular weight $\theta$, and the second moment of the fuel vapor distribution $\Psi$ are

$$\frac{\partial}{\partial t}(\rho y_F) + \nabla\cdot(\rho\vec{\mathbf{v}} y_F) = \nabla\cdot(\rho\overline{D}\nabla y_F) + \frac{d}{dt}(\rho y_F)^s \tag{3}$$

$$\frac{\partial}{\partial t}(\rho y_F\theta) + \nabla\cdot(\rho\vec{\mathbf{v}} y_F\theta) = \nabla\cdot(\rho\tilde{D}\nabla(y_F\theta)) + \frac{d}{dt}(\rho y_F\theta)^s \tag{4}$$

$$\frac{\partial}{\partial t}(\rho y_F\Psi) + \nabla\cdot(\rho\vec{\mathbf{v}} y_F\Psi) = \nabla\cdot(\rho\hat{D}\nabla(y_F\Psi)) + \frac{d}{dt}(\rho y_F\Psi)^s \tag{5}$$

where $\rho$ is the density of the gas mixture and $y_F$ is the mass fraction of the continuous fuel vapor. $\vec{\mathbf{v}}$ is the mass-averaged velocity of the gas phase mixture. $\overline{D}$, $\tilde{D}$ and $\hat{D}$ are diffusion coefficients associated with the diffusion processes of the vapor mass, the vapor mean molecular weight and the second moment of the vapor distribution respectively. Since the values of these coefficients are very close to each other [8], they are assumed to be equal. In this paper only source terms from the fuel spray, $\frac{d}{dt}(\rho y_F)^s$, $\frac{d}{dt}(\rho y_F\theta)^s$, $\frac{d}{dt}(\rho y_F\Psi)^s$ are considered, which are obtained from the liquid phase calculation and the exchange between the liquid phase and the vapor phase. The moments $\theta$ and $\Psi$ are defined as

$$\theta = \int_0^\infty f(I)IdI \tag{6}$$

$$\Psi = \int_0^\infty f(I)I^2dI \tag{7}$$

The energy equation can be derived and simplified as

$$\overline{C}_P\frac{\partial}{\partial t}(\rho T) + \overline{C}_P\nabla\cdot(\rho\vec{\mathbf{v}}T) = \nabla\cdot\lambda\nabla T + \left[(a_c - C_{PA})\rho\overline{D} + b_c\rho\theta\tilde{D}\right]\nabla y_F\cdot\nabla T \tag{8}$$

where $\overline{C}_P$ is the mixture specific heat, $T$ is the temperature, $\lambda$ is the thermal conductivity, $C_{pA}$ is the specific heat of air, $a_c$ and $b_c$ are the coefficients of a linear correlation of specific heat taken from Chou and Prausnitz [29] as a function of composition. The energy equation (8) is used for solving the droplet surface temperature, as described by Ra and Reitz [12].

#### Liquid phase governing equations

Assuming no absorption of ambient gas into the liquid droplet, a general form of the governing equation for the change rate of the various moments of the liquid fuel distribution is [12]

$$\frac{\rho_L R}{3}\frac{d\theta_L^{\,n}}{dt} = \dot{m}\frac{\theta_L^{\,1}}{\theta_V^{\,1}}(\theta_L^{\,n} - \theta_V^{\,n}) \qquad (n = 1,2,\cdots\cdots) \tag{9}$$

where $\rho_L$ is the mass density of the liquid fuel, $R$ is the droplet radius, $\theta_L^{\,n}$ and $\theta_V^{\,n}$ are the nth moments of the fuel distribution in the liquid phase and vapor phase respectively, as defined in equations (6) and (7), $\dot{m}$ is the vaporization mass flux. Substituting n=1 and n=2 into equation (9), the governing equation for the change rate of the first and second moments of the liquid phase composition can be obtained as

$$\frac{d\theta_L}{dt} = \frac{3\dot{m}}{\rho_L R}\frac{\theta_L}{\theta_V}(\theta_L - \theta_V) \tag{10}$$

$$\frac{d\Psi_L}{dt} = \frac{3\dot{m}}{\rho_L R}\frac{\theta_L}{\theta_V}(\Psi_L - \Psi_V) \tag{11}$$

The vaporization mass flux $\dot{m}$ is closely coupled with the source terms in the vapor phase transport equations (3)

to (5). Ra and Reitz showed the calculation of $\dot{m}$ in detail in [12]. The source terms in the vapor phase transport equations (4) and (5) can be derived as [6]

$$\theta^s = Y_{F,R}\theta_R - \frac{1}{B}(\theta_\infty Y_{F,\infty} - \theta_R Y_{F,R}) \tag{12}$$

$$\Psi^s = Y_{F,R}\Psi_R - \frac{1}{B}(\Psi_\infty Y_{F,\infty} - \Psi_R Y_{F,R}) \tag{13}$$

where $Y_{F,R}$ is the fuel vapor molar fraction at the droplet surface, $\theta_R$ and $\Psi_R$ are the mean molecular weight and the second moment of fuel vapor distribution at the droplet surface, $Y_{F,\infty}$ is the fuel vapor molar fraction at an infinite ambient, which can be approximated as the studied cell's value, $\theta_\infty$ and $\Psi_\infty$ are the mean molecular weight and the second moment of the fuel vapor distribution in the studied cell, $B$ is the Spalding number, which is calculated as

$$B = (Y_{F,R} - Y_{F,\infty})/(1 - Y_{F,R}) \tag{14}$$

The calculation of $Y_{F,R}$, $\theta_R$ and $\Psi_R$ will be shown later.

Distribution function and vapor-liquid equilibrium

The $\Gamma$ distribution function is chosen in this paper because of its ability to adequately represent petroleum fractions [8]. The $\Gamma$ distribution function for the liquid phase droplet is formulated as

$$f(I) = \frac{(I-\gamma)^{\alpha-1}}{\beta^\alpha \Gamma(\alpha)} \exp\left[-\left(\frac{I-\gamma}{\beta}\right)\right] \tag{15}$$

where $\alpha$ and $\beta$ are parameters that determine the shape of the distribution and $\gamma$ is the origin of the distribution function. The distribution function is molar-based for the droplet. In KIVA all calculations are mass-based for the gas phase. The conversion between the mass-based formulation and the molar-based formulation is

$$f_{mass}(I)dI = f_{molar}(I)\frac{I}{\theta_{molar}}dI \tag{16}$$

From the $\Gamma$ distribution function, the mean molecular weight (the first moment of the distribution function) $\theta$, the second moment $\Psi$, and the variance $\sigma^2$ in both the molar-base and mass-base are (assuming $\gamma$=0)

$$\begin{cases} \theta_{molar} = \alpha\beta \\ \Psi_{molar} = \alpha(\alpha+1)\beta^2 \\ \sigma_{molar}{}^2 = \alpha\beta^2 \\ \theta_{mass} = (\alpha+1)\beta \\ \Psi_{mass} = (\alpha+1)(\alpha+2)\beta^2 \end{cases} \tag{17}$$

In the continuous thermodynamics approach, the equilibrium at the interface between the liquid droplet and the surrounding gas is based on the assumption that the chemical potential for the liquid phase and the vapor phase are equal for each value of $I$. The fuel vapor mole fraction at the droplet surface can be determined by using Raoult's law as

$$Y_{FR} = \frac{P_{atm}}{P}\frac{\exp[A(1-\gamma B)]}{(1+AB\beta_L)^{\alpha_L}} \tag{18}$$

where $P_{atm}$ is the reference pressure of 101.325 kPa, $P$ is the pressure, $A$ and $B$ are functions of temperature from the integration of the composition-dependent Clausius-Clapeyron equation. The Clausius-Clapeyron equation is of the form

$$P^{sat}(I) = P_{atm} \cdot \exp\left[\frac{s_{fg}}{\overline{R}}\left(1 - \frac{T_B(I)}{T}\right)\right] \tag{19}$$

where $s_{fg}$ is the entropy of vaporization (which is expressed using Trouton's law as $s_{fg} = IL_V / T_B \approx 10.6\overline{R} \approx 87.9$, $L_V$ is the vapor latent heat of evaporation, $T_B$ is the boiling point temperature), $\overline{R}$ is the universal gas constant, $T_B$ is the normal boiling point temperature of component $I$, and $T$ is the droplet temperature. Assuming a linear variation of the normal boiling point temperature with composition $T_B(I) = a_B + b_B I$, with $a_B$ and $b_B$ constants obtained from regression of boiling data for the particular homologous family of components ($a_B$=208.53, $b_B$=1.5763), the vapor pressure can be expressed as

$$P^{sat}(I) = P_{atm} \cdot \exp[A(1 - B \cdot I)] \tag{20}$$

In this study, $A$ and $B$ are expressed as

$$A = \frac{s_{fg}}{\overline{R}}\left(1 - \frac{208.53}{T}\right), B = \frac{1.5763}{T - 208.53} \tag{21}$$

Using equations (17) to (21), a simple relation between the distribution parameters in the liquid and vapor phases can be obtained as [6]

$$\theta_V = \gamma + \frac{\theta_L - \gamma}{(1 + \frac{AB\sigma_L{}^2}{\theta_L - \gamma})}, \quad \sigma_V{}^2 = \sigma_L{}^2\left[\frac{\theta_V - \gamma}{\theta_L - \gamma}\right]^2 \tag{22}$$

Determination of surface temperature

For more accurate predictions of the vaporization rate and heat flux, a surface temperature calculation model was incorporated in the continuous multi-component (CMC) fuel model by Ra and Reitz [12]. The surface temperature of the droplet is determined from a heat and mass transfer balance at the interface between the droplet and the surrounding gas. The rate of heat transfer balances with the required heat for vaporization at the surface following

$$L(T_s)\dot{m} = q_i + q_o \tag{23}$$

where $L(T_s)$ is the latent heat of the fuel at the surface temperature $T_s$, $\dot{m}$ is the vaporization mass flux, $q_i$ is the heat transfer from inside the droplet, and $q_o$ is the heat transfer from outside of the droplet. Ra and Reitz gave the detailed calculation of $q_i$ and $q_o$ in both normal evaporation and boiling cases in Ref. [12]. Neglecting the effect of radiation, the temporal change of the droplet temperature is given as

$$\frac{dT_d}{dt} = \frac{Ah_{i,eff}(T_s - T_d)}{\rho c_v V} \text{ for normal evaporation} \quad (24)$$

$$\frac{dT_d}{dt} = \frac{A\alpha(T_b - T_d)}{\rho c_v V} \text{ for flash boiling} \quad (25)$$

where $\rho$ is the droplet density, $A$ and $V$ are the droplet surface area and volume, respectively, $c_v$ is the specific heat at constant volume of the liquid phase at the droplet temperature, $h_{i,eff}$ and $\alpha$ are the effective heat transfer coefficients for the normal evaporation and boiling cases, respectively, and $T_b$ is the boiling temperature. Equations (24) and (25) are solved implicitly in the computer code.

## G-EQUATION COMBUSTION MODEL AND ITS IMPROVEMENTS

### G-equation description of modeling premixed turbulent flame propagation

A G-equation combustion model for describing turbulent flame propagation has been developed and implemented into the KIVA-3V release2 code by Tan and Reitz [25,26]. Subsequently, consideration of detailed chemical kinetics was incorporated into the KIVA-3V release2 G-equation code to model the post-flame chemistry and end-gas auto-ignition chemistry by Liang and Reitz [22,23,24]. The G-equation combustion model is mainly based on the turbulent premixed combustion flamelet theory by Peters [14], where a set of Favre-averaged level-set equations was derived, including equations for the Favre mean, $\tilde{G}$, and its variance, $\tilde{G}''^2$, and a model equation for the turbulent/laminar flame surface area ratio $\sigma_T$, which, in turn, results in an explicit expression for the turbulent flame speed $S_T^0$. These equations, together with the Reynolds averaged Navier-Stokes equations and the turbulence modeling equations, form a complete set to describe premixed turbulent flame front propagation. The equation set suitable for implementation in CFD codes is [14,22,26]

$$\frac{\partial \tilde{G}}{\partial t} + (\tilde{\vec{u}} - \vec{u}_{vertex}) \cdot \nabla \tilde{G} = \frac{\overline{\rho}_u}{\overline{\rho}} S_T^0 \left|\nabla \tilde{G}\right| - D_T \tilde{k} \left|\nabla \tilde{G}\right| \quad (26)$$

$$\frac{\partial \tilde{G}''^2}{\partial t} + \tilde{\vec{u}} \cdot \nabla \tilde{G}''^2 = \nabla_{\|} \cdot \left(\frac{\overline{\rho}_u}{\overline{\rho}} D_T \nabla_{\|} \tilde{G}''^2\right) + 2D_T (\nabla \tilde{G})^2 - c_s \frac{\tilde{\varepsilon}}{\tilde{k}} \tilde{G}''^2 \quad (27)$$

$$\frac{S_T^0}{S_L^0} = 1 + I_P \left\{ -\frac{a_4 b_3^2}{2b_1}\frac{l_I}{l_F} + \left[ \left(\frac{a_4 b_3^2}{2b_1}\frac{l_I}{l_F}\right)^2 + a_4 b_3^2 \frac{u' l_I}{S_L^0 l_F} \right]^{1/2} \right\} \quad (28)$$

where $\tilde{\vec{u}}$ is the Favre-average fluid velocity; $\vec{u}_{vertex}$ is the mesh vertex velocity which accounts for mesh movement; $\nabla \tilde{G}$ is the gradient of $\tilde{G}$; $\nabla \tilde{G}''^2$ is the gradient of $\tilde{G}''^2$; $\overline{\rho}_u$ is the Reynolds-average of the unburned mixture density; $\overline{\rho}$ is the Reynolds-average of the cell gas density; $S_T^0$ is the turbulent flame speed; $D_T$ is the turbulent diffusivity; $\nabla_{\|}$ denotes the tangential gradient operator; $c_s$ is a modeling constant (cf. Ref. [14]); $\tilde{k}$ and $\tilde{\varepsilon}$ are the Favre mean turbulent kinetic energy and its dissipation rate from the RNG $k$-$\varepsilon$ model [30]; $u'$ is the turbulence intensity; $S_L^0$ is the laminar flame speed; $l_I$ and $l_F$ are the turbulence integral length scale and the laminar flame thickness, respectively; and $a_4$, $b_3$, $b_1$ are constants from turbulent flame speed model [14]. The term $I_P$ in Eq. (28), called a progress variable in Ref. [22], takes the form

$$I_P = \left[1 - \exp(-c_{m2}\frac{t - t_0}{\tau})\right]^{1/2} \quad (29)$$

where $c_{m2}$ is a model constant; $t_0$ is the spark timing; $\tau = \tilde{k}/\tilde{\varepsilon}$ is the turbulence time scale. Physically, the progress variable $I_P$ models the increasingly disturbing effect of the surrounding eddies on the flame front surface as the spark-ignition kernel flame grows from the laminar stage into the fully developed turbulent stage.

### The effect of residual on flame speed

The laminar flame speed correlation used is [Ref. 22]

$$S_L^0 = S_{L,ref}^0 \left(\frac{T_u}{T_{u,ref}}\right)^{\alpha} \left(\frac{p}{p_{ref}}\right)^{\beta} F_{dil} \quad (30)$$

where $S_{L,ref}^0$ is the laminar flame speed at a reference state, $T_u$ is the unburned mixture temperature, $T_{u,ref}$ is the unburned mixture temperature at the reference state, $p$ is the pressure, $p_{ref}$ is the reference pressure, and $\alpha$ and $\beta$ are correlated as functions of equivalence ratio. $F_{dil}$ is a factor that accounts for the presence of diluents, which can be expressed as

$$F_{dil} = 1 - f_{dil} Y_{dil} \quad (31)$$

where $f_{dil}$ is an experimentally determined constant, and $Y_{dil}$ is the "residual mass fraction", including $CO_2$, $H_2O$, residual $N_2$, and other residual components. From the above correlations, it is seen that the turbulent flame speed $S_T^0$ decreases as the "residual mass fraction" $Y_{dil}$ increases and the evaluation of turbulent flame speed is sensitive to the "residual mass fraction".

The effect of residual value on the flame speed can be seen in Figure 1 [31] and Figure 2 [32]. In Metghalchi and Keck's work, as shown in Figure 1, the effect of diluting stoichiometric isooctane-air mixtures with simulated combustion products was measured for an initial temperature $T_1$=298K and $P_1$=1 atm. A mixture of 15% carbon dioxide and 85% nitrogen by volume was used to simulate combustion products. This mixture has a molecular weight of 30.4 and a heat capacity which approximately matches that of the combustion products. In Figure 1, the ratio of the burning velocities with and without dilution are plotted as a function of unburned gas

temperature for diluent mass factions $Y_{dil}$=0.1 and $Y_{dil}$=0.2. It can be seen that the decrease in burning velocity ratio is independent of temperature and can be represented by the expression

$$S_u(Y_{dil}, T_u^0) / S_u(0, T_u^0) = 1 - 2.1 Y_{dil} \quad (32)$$

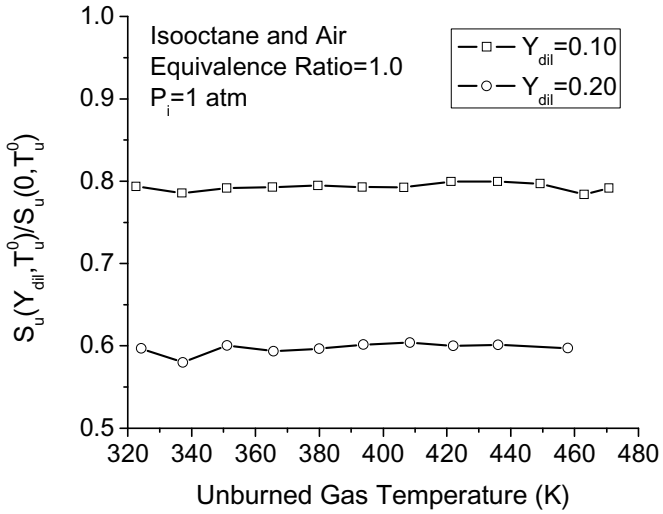


Figure 1 Effect of diluting stoichiometric isooctane-air mixtures with simulated combustion products [31]

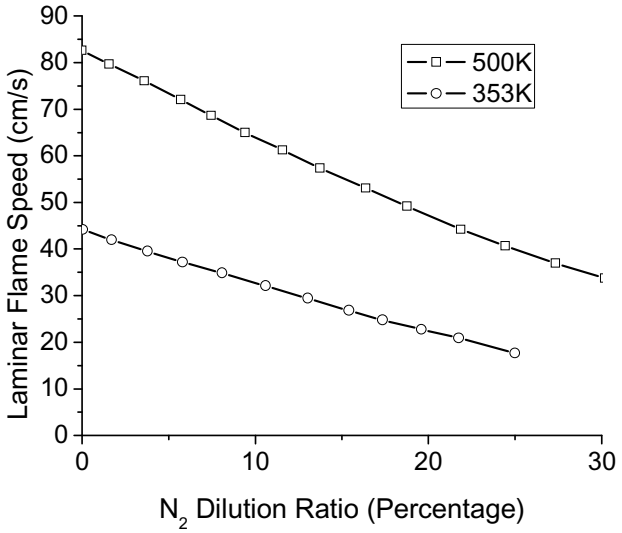


**Figure 2** Laminar flame speed of 87 octane gasoline at atmospheric pressure with $N_2$ dilution for equivalence ratio of 0.84 at 353 K and 500 K [32]

In Zhao et al.'s work, as shown in Figure 2, the dilution effect on the laminar flame speed was studied for 87 octane gasoline at 353 K and 500 K for equivalence ratio of 0.84 with $N_2$ as diluent. The laminar flame speeds in Figure 2 exhibit nearly linear dependencies on the dilution ratio.

For the engine simulation, the residual value of the cell at the location of the spark plug at the time of spark ignition was used in every cell in the combustion model of Liang [22,23,24]. However, the local and instantaneous residual value should be used for more accurate results. The effect of residual value on burning velocity for a GTDI engine simulation was studied by Yang et al. [27].

Transport equation residual model

Yang et al. [27] explored different methods to calculate the "residual mass fraction", including using the residual value in the cell at the location of the spark plug at the time of spark ignition and the overall residual value of the cylinder. An improved method to account for the local residual mass fraction was introduced. In this method (called "Resid_save") the local residual mass fraction distribution in the combustion chamber before spark ignition is stored into an array. During combustion, the stored local residual mass fraction for each cell is used to calculate the flame speed. The results showed that the "Resid_save" method was better than others. However this method only considers the "local" characteristics of the residual, and it does not consider the transport either by diffusion or by convection and source terms of residual. That means it does not consider the "instantaneous" characteristics of the residual. To accurately calculate the residual value distribution and to distinguish between burned gas combustion products that originate from the EGR gases and those from the current combustion event, a transport equation residual model was proposed by Yang et al. [28].

For N residual species each with density $\rho_{iR}$, we have

$$\sum_{i=1}^{N}\left[\frac{\partial \rho_{iR}}{\partial t} + \nabla\cdot\left(\rho_{iR}\vec{u}\right) = \nabla\cdot\left[\rho D \nabla \rho_{iR}\right] + \left(\dot{\rho}_{iR}\right)_{ChemK}\right]$$

$$\Rightarrow \frac{\partial \rho_{\sum_{i=1}^{N} iR}}{\partial t} + \nabla\cdot\left(\rho_{\sum_{i=1}^{N} iR}\,\vec{u}\right) = \nabla\cdot\left[\rho D \nabla \rho_{\sum_{i=1}^{N} iR}\right] + \sum_{i=1}^{N}\left(\dot{\rho}_{iR}\right)_{ChemK}$$

Defining a "pseudo" species, named "Ar", which is the $\sum_{i=1}^{N} iR$, and writing $\sum_{i=1}^{N}\left(\dot{\rho}_{iR}\right)_{ChemK}$ as $\left(\dot{\rho}_{Ar}\right)_{ChemK}$, the above equation becomes

$$\frac{\partial \rho_{Ar}}{\partial t} + \nabla\cdot\left(\rho_{Ar}\vec{u}\right) = \nabla\cdot\left[\rho D \nabla \rho_{Ar}\right] + \left(\dot{\rho}_{Ar}\right)_{ChemK} \quad (33)$$

Equation (33) is the final residual transport equation. To calculate the chemical source terms $\left(\dot{\rho}_{Ar}\right)_{ChemK}$, $\left(\dot{\rho}_{iR}\right)_{ChemK}$ of each species is calculated separately, then $\left(\dot{\rho}_{Ar}\right)_{ChemK}$ is the summation of $\left(\dot{\rho}_{iR}\right)_{ChemK}$ of all residual species. The initial amount of the "pseudo" species "Ar" actually is the summation of the assigned value of each residual species at the beginning of the calculation.

To solve the residual transport Eq. (33), $\nabla\cdot\left[\rho D \nabla \rho_{Ar}\right]$ is calculated in the species mass fraction iteration subroutine (in KIVA: "yit-transp.f"), and $\nabla\cdot\left(\rho_{Ar}\vec{u}\right)$ can be calculated in the advection flux calculation subroutine (in KIVA: "ccflux-transp.f"). As mentioned earlier, $\left(\dot{\rho}_{Ar}\right)_{ChemK}$ is the summation of $\left(\dot{\rho}_{iR}\right)_{ChemK}$ of all residual species. For the calculation of $\left(\dot{\rho}_{iR}\right)_{ChemK}$ CHEMKIN is called to calculate $\left(\dot{\rho}_{i}\right)_{ChemK}$ for each cell "*i4*" and because

$(\dot{\rho}_i)_{ChemK} = (\dot{\rho}_{iR})_{ChemK} + (\dot{\rho}_{iNotR})_{ChemK}$, we have

$(\dot{\rho}_{iR})_{ChemK} = (\dot{\rho}_i)_{ChemK} \times \frac{\rho_{Ar}}{\rho_{i4}}$.

It should be noticed that the equation of state is still $P = R_0 T \sum_{i=1}^{nsp} (\frac{\rho_i}{W_i})$, where "*nsp*" excludes the fictitious species "Ar", because the $\rho_i$ is already the density of the all "*i*" species, which includes the residual part of the species "*i*". It should also be noticed that in both the species mass fraction iteration subroutine and the flux calculation subroutine, the diffusion and convection of the "pseudo" species "Ar" do not contribute to the mass and enthalpy change of the computed cell, because the diffusion and convection are already calculated for each species "*i*".

After solving the residual transport equation, the "residual mass fraction" can be calculated as $Y_{dil} = \rho_{Ar} / \rho_{i4}$ in each computational cell.

Damkohler number criterion for combustion regime in flame containing cells

In previous implementations of the G-equation combustion model with detailed chemical kinetics in Refs. [22,23,24], once a flame front cell is identified, the G-equation flame propagation method in which the chemical equilibrium solver is applied, is used for the calculation of species density change and energy release, and CHEMKIN is used in front of and behind the flame-containing cells. A new criterion was used to choose between the CHEMKIN and G-equation models in the flame front region by Yang et al. [28] and Tamagna et al. [33]. In this criterion a Damkohler number is introduced that is the ratio between the laminar flame propagation timescale and a chemical timescale. These time scales are used to evaluate, for every computational cell in the flame front region, whether combustion is locally controlled by flame propagation (e.g., flamelets) or by volumetric heat release.

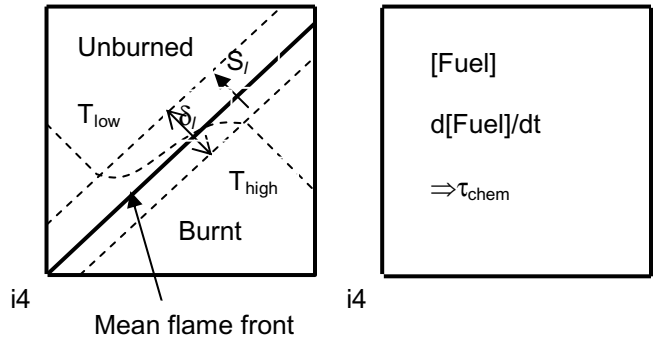


**Figure 3** Damkohler number criterion for combustion regime in flame containing cells

The Damkohler equation is defined as (refer to Figure 3)

$$Damk = \frac{\tau_{lam}}{\tau_{chem}} \tag{34}$$

where

$$\tau_{lam} = \frac{D_l}{S_l^2} = \frac{\delta_l}{S_l} \quad and \quad \tau_{chem} = \frac{[Fuel]}{d[Fuel]/dt} \tag{35}$$

and $D_l$ is the laminar diffusivity, $S_l$ is the laminar flame speed, $\delta_l$ is the laminar flame thickness, and $[Fuel]$ is the effective fuel concentration (i.e., fuel+CO+$H_2$ species). Note that the use of the laminar time scale (based on the laminar flame speed and diffusivity) is consistent with the interpretation that at a subgrid level flamelets control the combustion rate. In the case that flame propagation is dominant (bigger chemical timescale) the G-equation model is used for the combustion calculation in that cell. Otherwise (bigger laminar timescale) CHEMKIN is adopted to compute the combustion rate and energy release.

## PRF-ADAPTIVE MODEL FOR INTEGRATING THE CMC FUEL MODEL AND THE G-EQUATION COMBUSTION MODEL

In the continuous multi-component (CMC) model described earlier, the fuel composition is represented by a probability density function (PDF) or distribution function. In the calculation the mean molecular weight (the first moment of the distribution function) $\theta$, the second moment $\Psi$, and the variance $\sigma^2$ can be tracked. However this kind of composition representation is just an "abstract" composition representation, and it is not convenient for the combustion calculation in KIVA. In the CMC model, which has been implemented into KIVA [6,7,9,12], although the fuel composition in terms of $\theta$, $\Psi$, and $\sigma^2$ is already obtained, $\rho_1$ is the total density of all fuel species. But the real quantity of each fuel species is needed in the combustion calculation after fuel evaporation. To track the "actual" fuel composition, a PRF-adaptive model is introduced in this paper. In this model, to consider the change of local fuel vapor mixture composition, a relationship between the fuel vapor mixture PRF number (or Octane number) and the fuel vapor mixture composition based on the mean molecular weight and variance of the fuel vapor mixture composition in each cell is formulated. This model is described as follows.

The cetane number (CN) has been measured for a variety of pure hydrocarbons [34]. The data for paraffins (alkanes) is shown in Figure 4. The cetane number increases with molecular weight up to octadecane (MW=254.48, CN=110) after which no further increase is observed. This data was curve-fit with a third order polynomial ($R^2$=0.9878) which can be written as

$$CN_{par} = 29.295 + 0.14675 \times \theta + 1.7080 \times 10^{-3} \times \theta^2 - 4.2438 \times 10^{-6} \times \theta^3 \tag{36}$$

where $\theta$ represents the mean molecular weight of the vapor distribution.

The CN is evaluated based on the mean molecular weight of the computational cell composition distribution. It should be noted, however, that Eq. (36) cannot be used directly as a calculation of the cetane number in the computational cell because the gasoline fuel vapor exists as a blend of many components, which have not been taken into account explicitly [6]. Hence the cetane number was adjusted to account for the composition by means of a second correction, also shown in Figure 4. Before the adjustment, a relation between the cetane number (CN) and the research octane number (RON) which was proposed by Kalghatgi [35] is introduced, viz.,

$$CN = 54.6 - 0.42 \times RON \quad (37)$$

In Kalghatgi's work [35], cetane numbers were measured for PRFs using the ASTM D613 (engine) method, and the measured cetane numbers were plotted against RON. For DF2 (diesel fuel #2) the PRF (RON) is 29, according to equation (37), the cetane number of DF2 is

CN=54.6-0.42×29=42.42.

Thus the second correction can be constructed such that gasoline (MW=85.5) yields a CN of 14.532, and DF2 (diesel fuel #2 with MW=185.0) yields a CN of 42.42. This correlation is based on the data of Table 1, and can be expressed as

$$CN = 14.532 + 0.767123 \times (CN_{par} - 51.676) \quad (38)$$

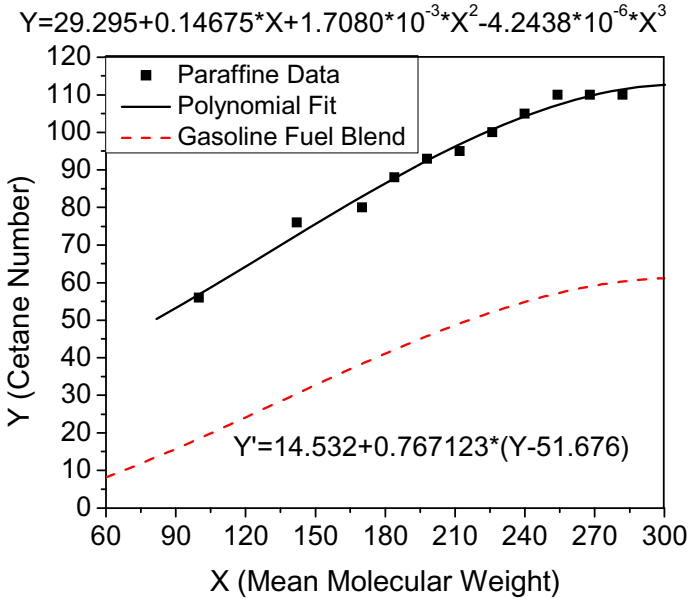


**Figure 4** Cetane number as a function of paraffin (alkane) molecular weight (after Rose and Cooper [34])

**Table 1** Parameters for different fuels

| Fuel | Gasoline | DF2 (Diesel fuel #2) |
|---|---|---|
| Mean Molecular Weight | 85.5 | 185.0 |
| RON | 95.4 | 29 |
| CN | 14.532 | 42.42 |
| CNpar | 51.676 | 88.030 |

Inserting equation (36) into equation (38) gives

$$CN = 14.532 + 0.767123 \times (-22.381 + 0.14675 \times \theta + 1.7080 \times 10^{-3} \times \theta^2 - 4.2438 \times 10^{-6} \times \theta^3)$$

and with equation (37) gives

$$RON = 136.279 - 0.268\theta - 0.00312\theta^2 + 0.00000775\theta^3 \quad (39)$$

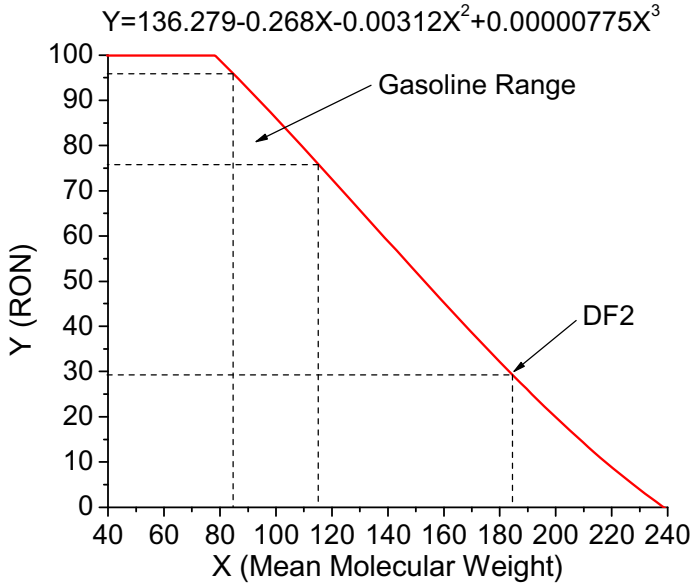


**Figure 5** RON as a function of computational cell fuel vapor mixture mean molecular weight

Equation (39) is a relationship between the fuel vapor mixture PRF number (or Octane number) and the fuel vapor mixture composition based on the mean molecular weight of the fuel vapor mixture composition in each cell. Equation (39) is shown in Figure 5. Because the CMC model traces the mean molecular weight (the first moment of the distribution function) $\theta$ of each cell, the octane number of the fuel vapor mixture can be calculated. For gasoline, mole fractions of iso-octane and n-heptane are assigned in each cell for modeling the combustion process.

## NEW LAMINAR FLAME SPEED CORRELATION FOR MULTI-COMPONENT FUEL

In the laminar flame speed correlation of equation (30), $S^0_{L,ref}$ is the laminar flame speed at a reference state, $\alpha = 2.18 - 0.8(\phi - 1)$, $\beta = -0.16 + 0.22(\phi - 1)$. However equation (30) and the correlation for $S^0_{L,ref}$ [22,23,24] apply for iso-octane. To consider multi-component fuel effects, the laminar flame speed correlation should be updated. Also, to prevent the flame speed from becoming negative at high residual mass fraction the correlation for $F_{dil}$, equation (31), was modified.

Experimental laminar flame speeds of different PRF mixtures at the reference condition have been obtained by Huang and Davis et al. [36], as shown in Figure 6(a). Based on these experimental laminar flame speed data, the laminar flame speed at the reference state was curve-fit for different PRF number as

$$S^0_{L,ref} = 34.1\phi^{-0.134}\exp(-3.86(\phi-1.146)^2) + (0.13482\phi - 0.09752\phi^2 + 0.01746\phi^3)(100 - PRF) \quad (40)$$

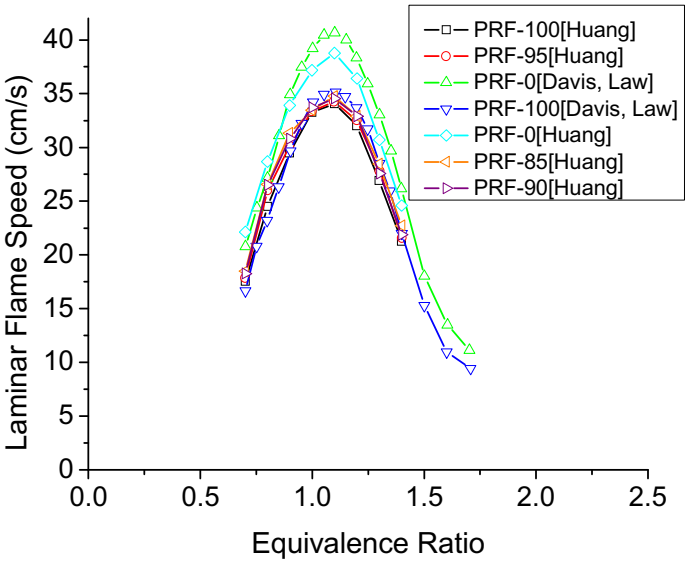


**(a)** Experimental data

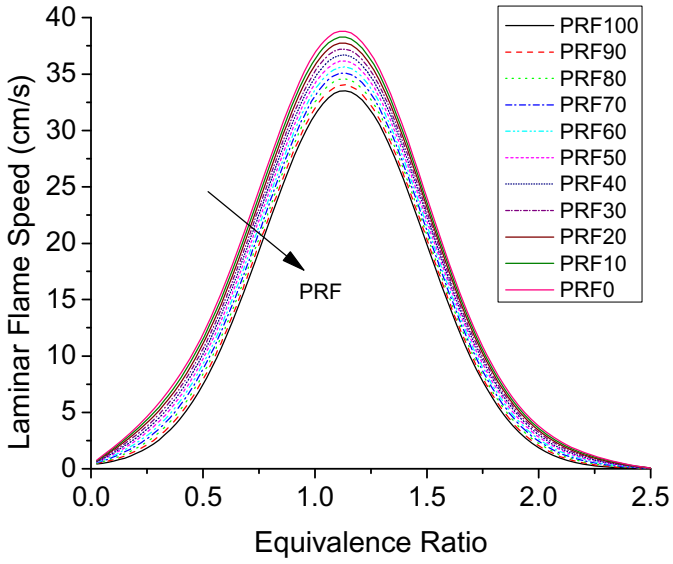


**(b)** Equation (40)

**Figure 6** Comparison between the new laminar flame speed correlation and the experimental data

The range of equivalence ratio, $\phi$, in equation (40) is 0.0 to 2.5. Equation (40) is shown in Figure 6(b). From a comparison between Figure 6(a) and Figure 6(b), it is seen that the laminar flame speeds at the reference condition from equation (40) are close to the experimental laminar flame speeds for each PRF number.

The correlation for $F_{dil}$ was modified as

$$F_{dil} = (1 - Y_{dil})^{(a+bY_{dil}+cY_{dil}^2)} \quad (41)$$

where $Y_{dil}$ is the residual mass fraction, and a=2.1, b=-0.6, c=21.85. Figure 7 shows different correlations for calculating the effect of residual mass fraction $Y_{dil}$ on $F_{dil}$. From Figure 7, it is seen that $F_{dil}$ from correlation (41) is always positive.

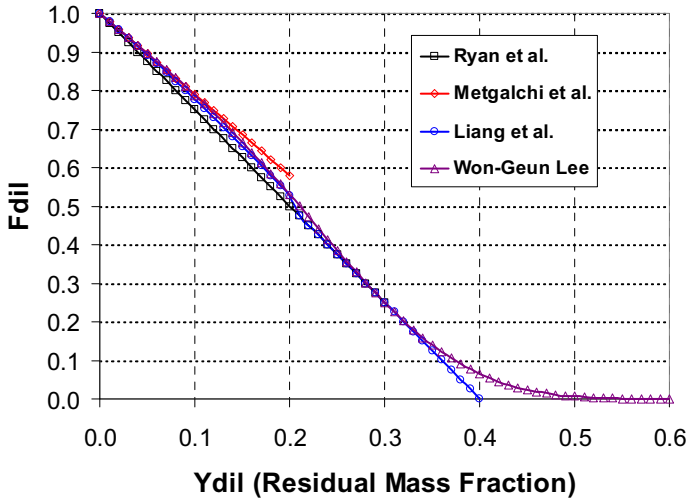


**Figure 7** Comparison of different residual effect correlations

## NEW PRF MECHANISM FOR MODELING CHEMICAL KINETICS

As mentioned earlier, detailed chemistry is used to simulate the low-temperature auto-ignition process of the end-gas. Each computational cell ahead of the flame front is modeled as a WSR (Well-Stirred-Reactor) for calculating the chemistry source terms of the species and energy transport equations. The WSR approximation has been proven to be an effective way of modeling HCCI combustion in several previous studies [38,39]. In the present model, the CHEMKIN code [40] is used for solving the detailed chemical kinetics mechanisms.

In Liang's study [22,23,24], a 22-species, 42-reactions *iso*-octane ($iC_8H_{18}$) mechanism, which was extracted from a 32-species, 55-reactions primary reference fuel (PRF) mechanism by Tanaka et al. [41], was adopted to model the auto-ignition process of the gasoline/air/residual-gas mixture ahead of the flame front in gasoline SI engines. This PRF mechanism was originally validated in a rapid compression machine (RCM) for fuel-lean mixtures over a wide range of initial temperature and pressure conditions, where the maximum equivalence ratio studied was 0.5 [41]. In Liang's work [22,23,24], the mechanism was further

reduced and further validated for both lean and rich mixtures by comparing calculated ignition delay times with experimental data obtained from the shock-tube measurements by Fieweger et al. [42].

The MIT PRF mechanisms [41] match of ignition delay between experimental data and simulation results deteriorates for rich mixtures and low PRF mixtures. Recently Ra and Reitz [43] have developed a reduced chemical kinetic mechanism for the oxidation of primary reference fuels (PRF) and applied it to model internal combustion engines. The final version of this PRF mechanism consists of 41 species and 130 reactions. This new PRF mechanism was validated and used in this paper.

## RESULTS

### CODE DEVELOPMENT

In the present ERC-KIVA-3V release2 code, the continuous multi-component (CMC) fuel evaporation model was integrated with the improved G-equation combustion and detailed chemical kinetics model. In the integration, the "PRF adaptive" described above method was used. The updated laminar flame speed correlation was also implemented into the code. The new PRF mechanism was used for gasoline engine simulation.

### VALIDATION OF THE CONTINUOUS MULTI-COMPONENT (CMC) FUEL MODEL

The continuous multi-component (CMC) fuel evaporation model was applied to study single stagnant droplet evaporation and spray evaporation in a cylindrical chamber.

#### Single stagnant droplet evaporation

In the simulation of an evaporating single droplet, the parameters of the $\Gamma$ distribution function were chosen as shown in Table 2 for the composition of gasoline and iso-octane in the multi-component fuel model.

**Table 2** Fuel distribution parameters

| Fuel | Gasoline | Iso-octane |
|---|---|---|
| $\alpha$ | 5.7 | 100 |
| $\beta$ | 15 | 0.1 |
| $\gamma$ | 0 | 104.2 |
| $\theta$ | 85.5 | 114.2 |
| $\sigma$ | 35.8 | 1 |

The simulation results for normal evaporation of gasoline droplets are shown in Figure 8(a,b,c). In Figure 8 the initial ambient temperature and pressure are 1000 K and 1.0 bar, respectively, and the initial temperature and size of the droplet are 300 K and 100 $\mu$m, respectively. Because of preferential vaporization of the highly volatile light-end components in the gasoline composition, the mean molecular weight of the composition increases and

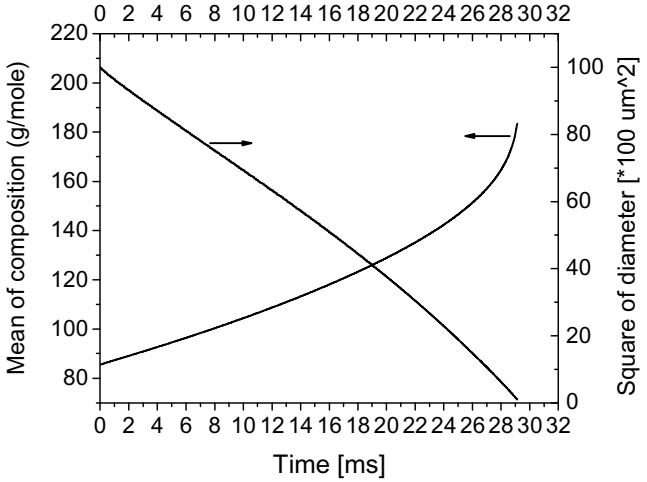


**(a)** Mean of composition and square of diameter of single droplet evaporation

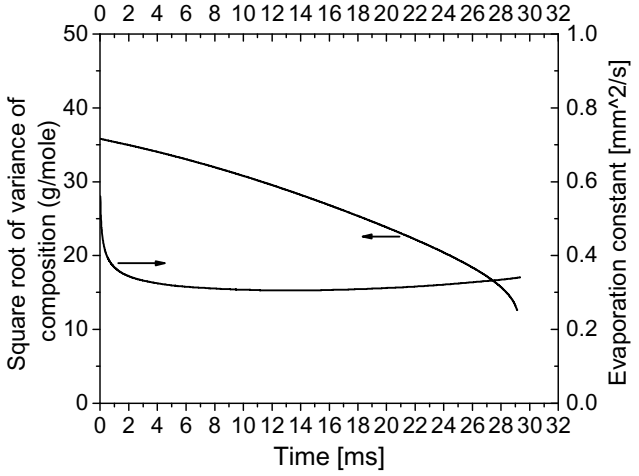


**(b)** Square root of variance of composition of the droplet and the evaporation constant

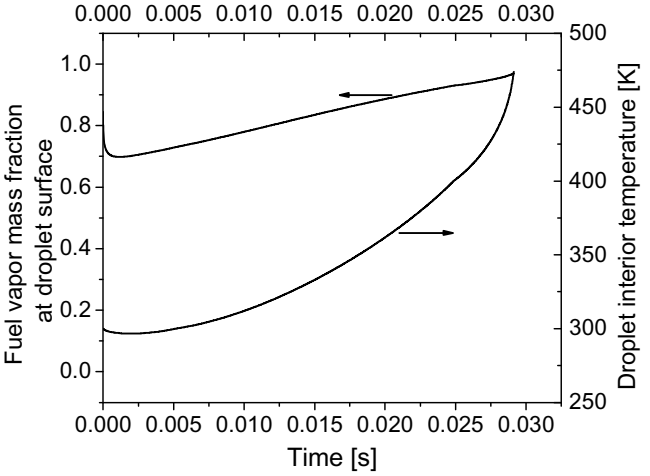


**(c)** Fuel vapor mass fraction at the droplet surface and droplet interior temperature

**Figure 8** Evaporation of a stagnant gasoline droplet in quiescent ambient air

the variance decreases steadily. The mass fraction of fuel vapor at the droplet surface decreases initially due to the increase of the mean of composition and the decrease of the surface temperature; it then increases because the heating effect is more than the reducing effect of the increase of the mean of composition.

Figure 9 shows a comparison of the predicted history of the droplet interior temperatures for gasoline and iso-octane droplets at ambient air pressures of 0.3 and 1.0 bar. The ambient temperature is 500 K, the initial droplet temperature is 300 K, and the initial droplet diameter is 100 μm. The gasoline droplet at the ambient pressure of 0.3 bar is vaporized through flash boiling initially and the other cases are in the normal evaporation mode. The gasoline droplets initially experience a cooling process, while the iso-octane droplets are heated up from the beginning [12]. Figure 9 also shows an interesting characteristic of multi-component fuel vaporization: gasoline droplets do not reach an equilibrium temperature as in the case of the single-component iso-octane droplet, because the composition of the droplets is continuously changing as the more volatile components are vaporized.

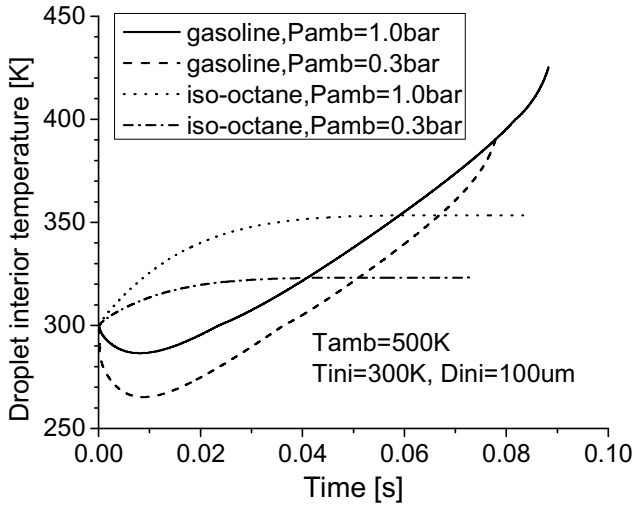


**Figure 9** Predicted history of the droplet interior temperature for gasoline and iso-octane droplets

Figure 10 shows the comparison of surface regression profiles for two ambient temperatures for gasoline and iso-octane droplets: 500K and 1000K. In Figure 10, the ambient pressure is 1.0 bar, the initial droplet temperature is 300 K, and the initial droplet diameter is 100 μm. From Figure 10, it is seen that as the ambient temperature increases the life time of the droplet decreases. Because the highly volatile light-end components in the gasoline composition evaporate preferentially, the gasoline droplet size decreases rapidly at the initial stage. However, compared with the iso-octane the evaporation rate of gasoline slows down in the late stage.

Figure 11 shows the corresponding evolutions of droplet interior temperature and surface temperature for gasoline and iso-octane droplets. For iso-octane, initially the surface temperature is higher than the interior temperature, and then there is an equilibrium drop temperature at which the interior and surface temperatures of the drop become equal when no heat transfer between the interior and the surface of the drop occurs. For gasoline, because of the evaporation at the surface, the cooling process of the surface is more obvious than the droplet interior, so the initial surface temperature is lower than the interior temperature. Then as it is heated up by the ambient gas, the surface temperature is higher than the interior temperature. Finally, the surface temperature is equal to the interior temperature. However, as mentioned above, the gasoline droplet does not reach an equilibrium temperature.

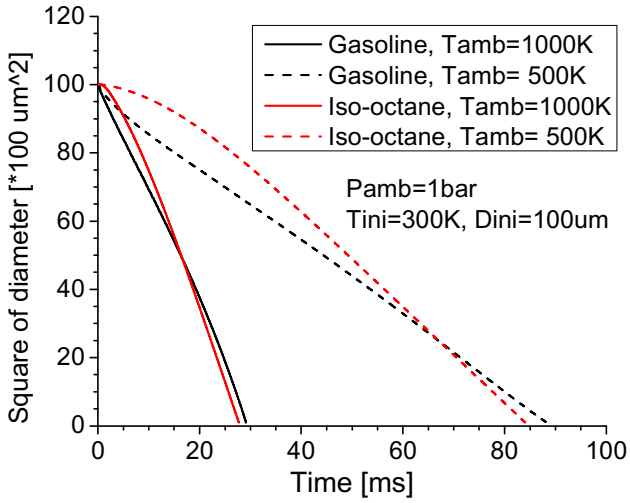


**Figure 10** Comparison of surface regression profiles for gasoline and iso-octane at two ambient temperatures

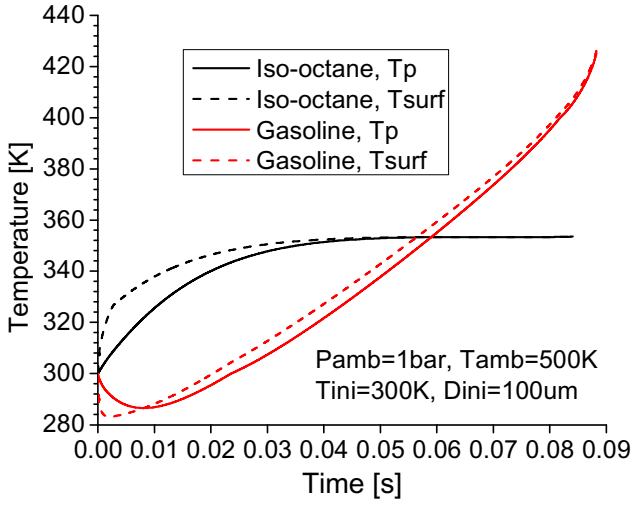


**Figure 11** Comparison of profiles of droplet interior temperature and surface temperature of iso-octane and gasoline vaporization

Spray evaporation in a cylindrical chamber

The CMC model was also applied to simulations of solid cone sprays injected into a cylindrical chamber. Detailed

specifications of the chamber and the injection parameters are listed in Table 3.

**Table 3** Chamber specifications and injection parameters for the spray simulations

| Parameters | Value |
|---|---|
| Chamber Bore (cm) | 14.0 |
| Chamber Height (cm) | 10.0 |
| Number of Injector Holes | 1 |
| Hole Diameter (cm) | 0.0153 |
| Spray Cone Angle (degree) | 30 |
| Injection Duration (degree) | 16.0 |
| Injection Amount (mg) | 13.6 |

The evaporation of multi-component gasoline sprays and single-component iso-octane sprays was considered. In both cases, the physical properties of the liquid fuel were set to those of iso-octane. The ambient conditions were 500 K and 0.5 bar, 1.0 bar, 1.5 bar and 2.0 bar. An initial droplet temperature of 360 K was used for simulating boiling evaporation of the spray droplets, since, based on the stagnant droplet vaporization results at 0.5 bar, the boiling temperatures of the iso-octane and gasoline droplets are 348.7 and 286.3 K, respectively [12]. Predictions of the shape and position of the gasoline spray using the continuous multi-component (CMC)

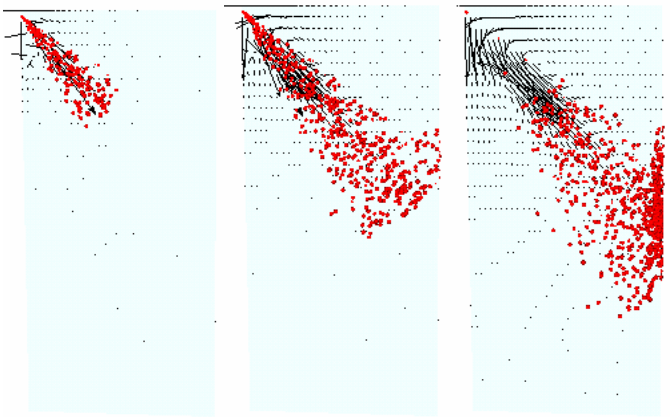


**(a)** Ambient pressure 2.0 bar

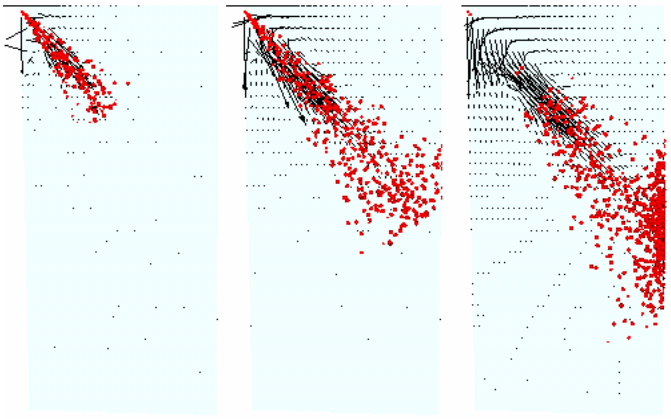


**(b)** Ambient pressure 1.5 bar

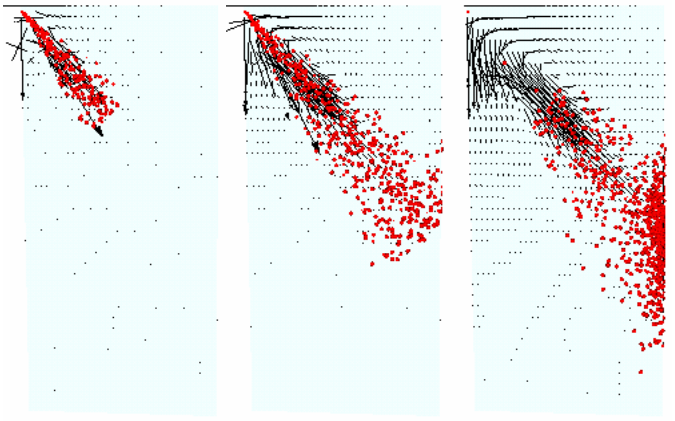


**(c)** Ambient pressure 1.0 bar

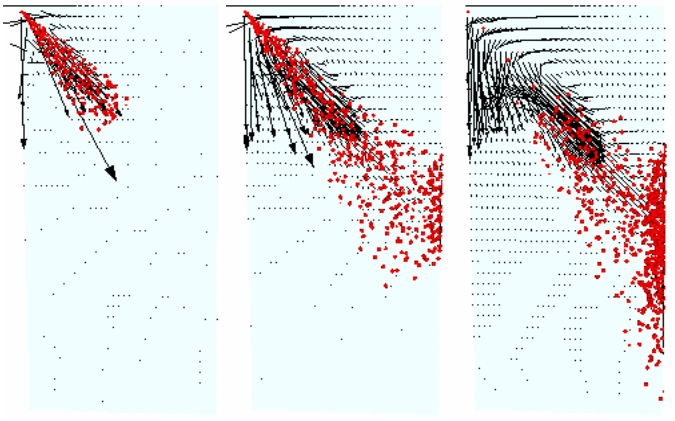


**(d)** Ambient pressure 0.5 bar

**Figure 12** Cross-section view of the flow field and droplet distribution of gasoline sprays at various times; Planes cross through the axis of the spray

model are shown in Figure 12. In the calculations, the speed was set as 1666.7 rev/min, thus the crank angle "CA" denotes the elapsed time.

From Figure 12, it is seen that as the ambient pressure decreases, the penetration length increases, the cone angle decreases, and most of the droplets move along a straight line without being influenced very much by the flow of the gas mixture. For the ambient pressure 0.5 bar case, because there exists flash-boiling, the droplet spatial distribution is more scattered. The first drop radius and total parcel number at the last crank angle of the ambient pressure 2.0 bar, 1.5 bar, 1.0 bar, 0.5 bar cases are 0.0072788 cm, 1197, 0.007199 cm, 1196, 0.0071775 cm, 1191, 0.0071002 cm, 1184, respectively. Because the drop size, parcel number, and ambient pressure decrease, the velocity increases. As the ambient density increases, the drag force increases and thus the droplets lose their initial momentum more quickly, and both the radial and axial penetrations decrease.

Figure 13 shows predictions of the shape and position of the iso-octane spray using the continuous multi-

component (CMC) model. The ambient conditions are the same as in Figure 12. From Figure 13 it is seen that the shape and positions of the spray are similar to those of the gasoline cases, but the iso-octane cases show a little less scattered spatial distribution. The reason is that the lighter components in the multi-component fuel vaporize preferentially and the heavier components, which are not readily vaporized remain in the droplets, and these partially vaporized droplets, which have smaller sizes are more easily affected by the induced gas flow. Compared with iso-octane the gasoline droplet

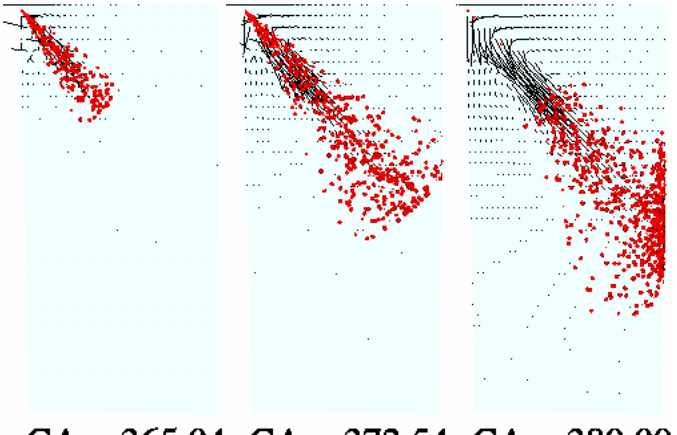


**(a)** Ambient pressure 2.0 bar

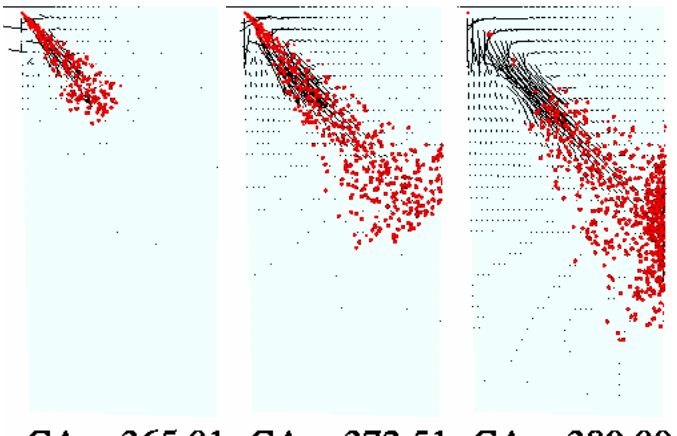


**(b)** Ambient pressure 1.5 bar

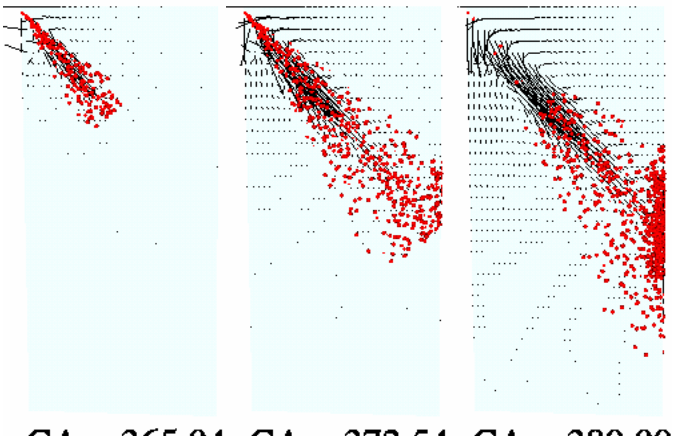


**(c)** Ambient pressure 1.0 bar

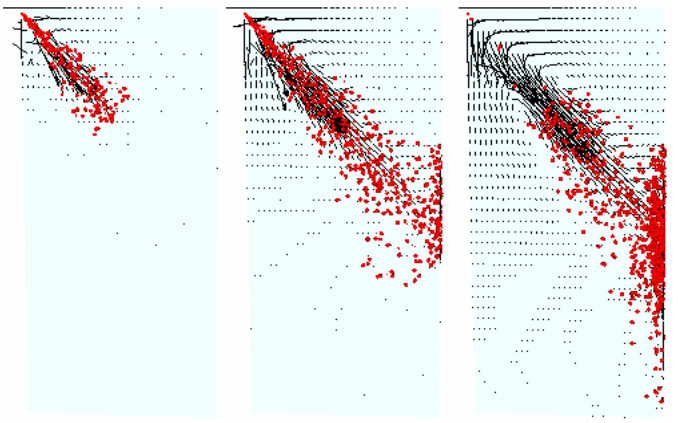


**(d)** Ambient pressure 0.5 bar

**Figure 13** Cross-sectional view of the flow field and droplet distribution of iso-octane sprays at various times; Planes cross through the axis of the spray

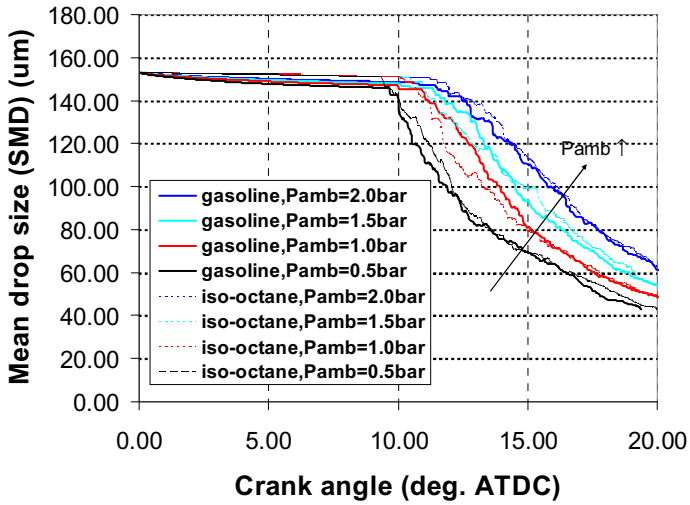


**(a)** Mean drop size

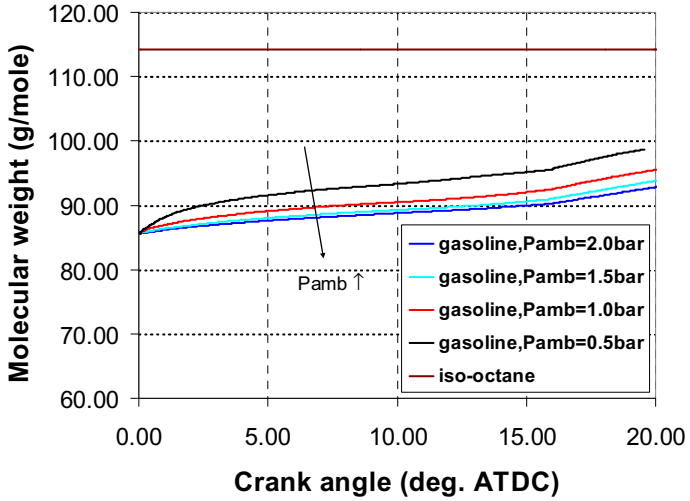


**(b)** Average molecular weight

**Figure 14** Temporal history of the mean drop size (SMD) and average molecular weight of gasoline and iso-octane sprays

size decreases more rapidly, so the drop velocities in Figure 12 is higher than those in Figure 13.

In Figure 14, the corresponding temporal changes of the mean drop size (Sauter mean diameter, or SMD) and mass-averaged molecular weight of the gasoline and iso-octane sprays are shown. Figure 15 shows the corresponding temporal history of the vaporized fraction of the gasoline and iso-octane sprays.

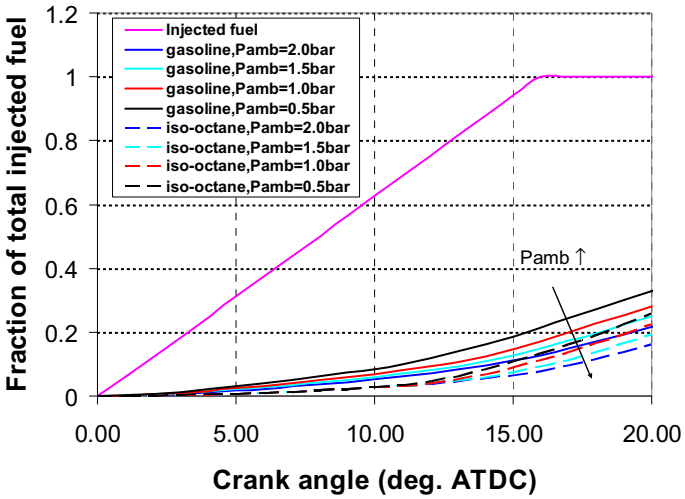


**Figure 15** Comparison of fuel distribution in the cylinder of the gasoline and iso-octane sprays

From Figure 14 and Figure 15, it is seen that: for each ambient pressure, the vaporized fraction of the gasoline spray is larger than that of the iso-octane spray; decreasing the ambient pressure is a favorable factor for the vaporization of the spray droplets; the average molecular weight of the gasoline spray increase steadily because more volatile light-end components of the gasoline fuel leave the droplets and heavier components remain in the droplets, whereas the single-component iso-octane has a constant value.

## VALIDATION OF THE G-EQUATION COMBUSTION MODEL AND ITS IMPROVEMENTS

### Validation of the new PRF mechanism

Ignition delay experiments using a RCM or a shock tube are commonly used to evaluate the auto-ignition tendencies of fuel/air mixtures, and to provide data for validating chemical kinetics mechanisms. In the shock tube experiment by Fieweger et al. [42], the ignition delay time is marked by an explosion of the bulk mixture following an inhomogeneous, deflagrative mild ignition. This “explosion” features dramatic temperature and pressure jumps in the shock tube due to chemical heat release. In the present calculation, the SENKIN code was used to compute the ignition delay times of the new PRF mechanism. The validation results for the new PRF mechanism are shown in Figure 16, Figure 17, and Figure 18.

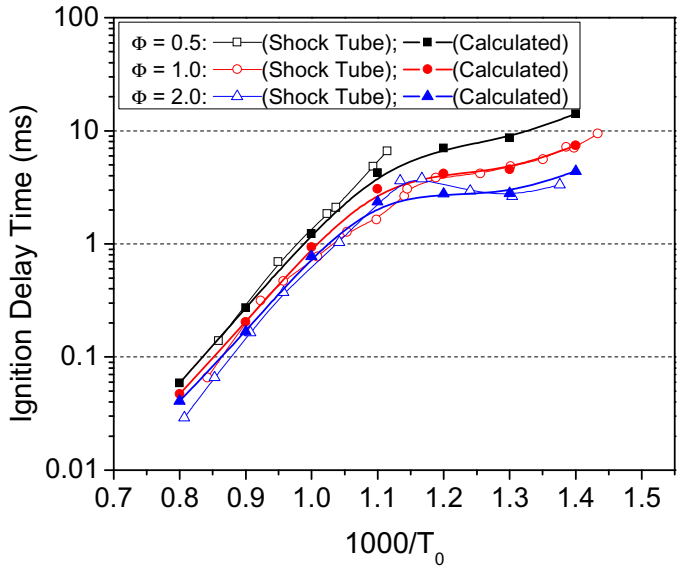


**Figure 16** Comparison of ignition delay time of iso-octane/air mixtures with different equivalence ratios (Initial pressure = 40 bar, $T_0$ is the initial temperature.)

Figure 16 shows ignition delay comparisons for *iso*-octane/air mixtures with three different equivalence ratios ($\Phi$= 0.5, 1.0, 2.0). The initial temperature $T_0$ ranges from around 700 K to 1250 K, with initial pressure fixed at 40 bar, which are typical conditions in SI engine operation. Compared to the measured data, the calculated values show similar trends for the equivalence ratio dependency, i.e., ignition occurs earlier with an increase of equivalence ratio for the same initial temperature and pressure conditions, except that the shock tube data shows some overlap between the $\Phi$ = 1.0 and $\Phi$ = 2.0 curves when $T_0$ ranges from 800 K to 1000 K.

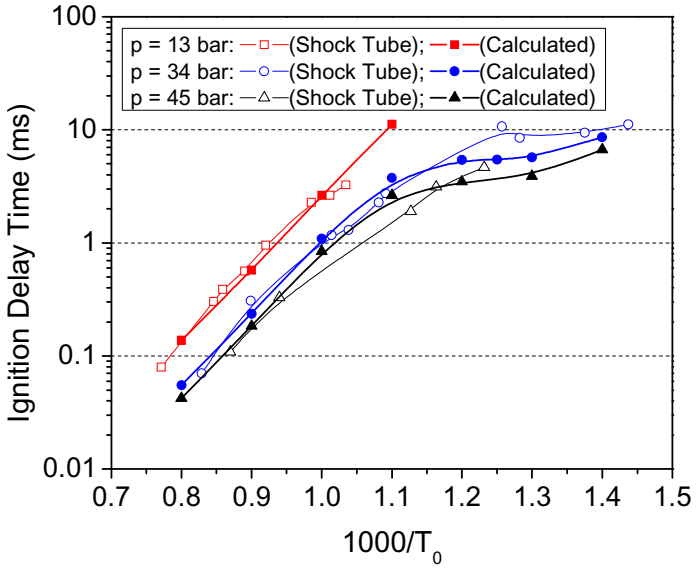


**Figure 17** Comparison of ignition delay time of iso-octane/air mixtures at different initial pressures ($T_0$ is the initial temperature, equivalence ratio $\Phi$ = 1.0)

Figure 17 shows the comparison for stoichiometric *iso*-octane/air mixtures at three different initial pressure levels. Similarly, the increasing auto-ignition tendency of *iso*-octane/air mixtures with increasing initial pressure is well captured in the calculations.

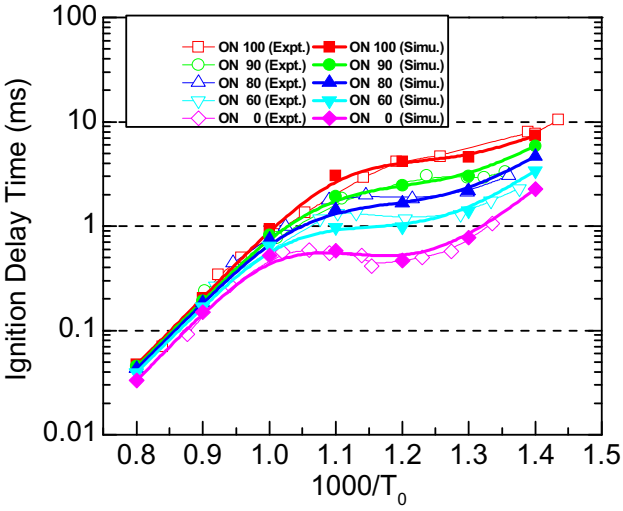


**Figure 18** Comparison of ignition delay time of iso-octane, n-heptane, and air mixtures at different octane numbers ($T_0$ is the initial temperature, equivalence ratio $\Phi$ = 1.0)

Figure 18 shows the comparison for stoichiometric *iso*-octane, n-heptane, and air mixtures at five different octane numbers. Similarly, the increasing auto-ignition tendency of *iso*-octane, n-heptane, and air mixtures with decreasing octane number for all initial temperatures is well captured in the calculations. From Figures 16, 17, and 18, it is seen that the calculated ignition delay times agree very well with the shock tube data.

The G-equation combustion model and its improvements were also tested with a pancake-shaped combustion chamber engine and a GTDI engine.

Pancake-shaped combustion chamber engine

To test the G-equation combustion model, computations were performed by Tan et al. [44] in a premixed charge SI engine. The spark plug is located at the center of the cylinder head, as shown in Figure 16. Four heat-flux probes (HT1-4) were situated on the engine head at 18.7, 27.5, 37.3, and 46.3 mm from the cylinder axis, and one probe (HT5) was located on the cylinder liner, 6.3 mm from the head, to measure the heat flux, as shown in Figure 16. The measured wall heat flux data were used to validate the G-equation combustion model. Figure 17 and Figure 18 show the measured and predicted heat fluxes, respectively. In general, the agreement between the predicted and measured data is satisfactory in terms of its phasing. For every probe, the flame arrival time at which the predicted heat flux increases sharply is almost the same as the corresponding time of the measured data. This indicates that the flame propagation speed is well predicted by the present G-equation combustion model.

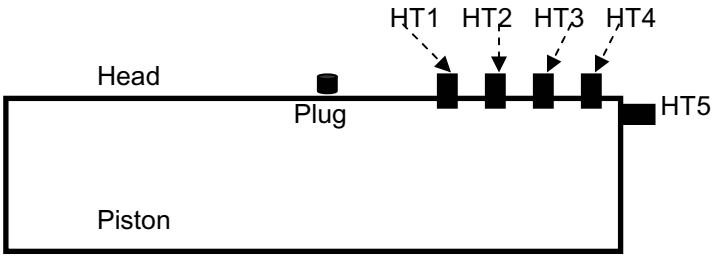


**Figure 19** Locations of the spark plug and heat flux probes in the pancake engine [44]

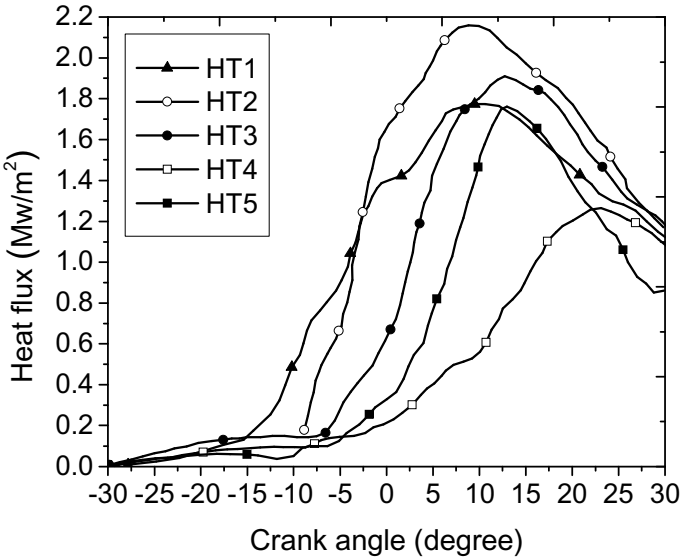


**Figure 20** Heat flux measured by probe HT1, HT2, HT3, HT4, and HT5 [44]

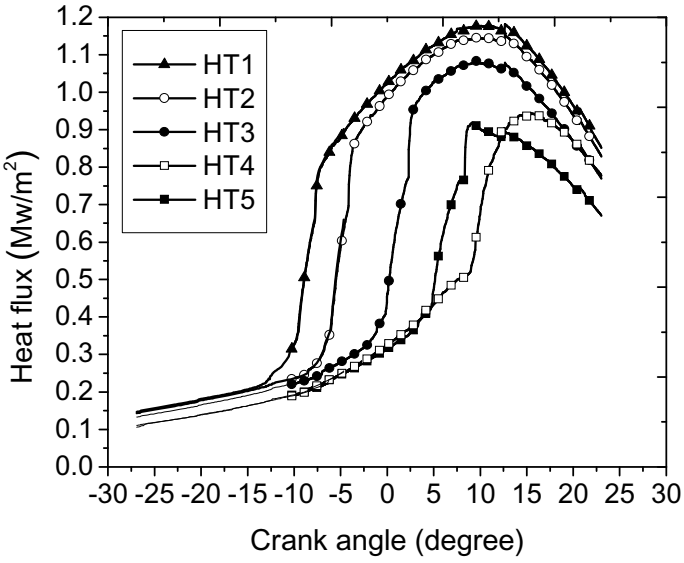


**Figure 21** Predicted heat flux for probe HT1, HT2, HT3, HT4, and HT5 [44]

Results from the transport equation residual model

To test the transport equation residual model, computations were performed by Yang et al. [28] for a Gasoline Turbocharged Direct Injection (GTDI) engine operated at two conditions. One operating condition is a high-load, uniform-mixture case (2000 rev/min, boosted charge), and the other one is low-load, uniform-mixture case (1500 rev/min). The specifications of the engine and the modeled operating conditions are listed in Table 4.

**Table 4** Specifications and operating conditions of the GTDI engine [28]

| Operating Conditions | High load | Low load |
|---|---|---|
| Bore / Stroke (mm) | 92.5 / 86.7 | |
| Connecting Rod Length | 152.4 mm | |
| Compression Ratio | 9.7 | 10.09 |
| Engine Speed (rev/min) | 2000 | 1500 |
| Spark Timing (° ATDC) | -11 | -37 |
| Overall Residual (%) | 1.8 | 25 |
| MAP (kPa) | 165.3 | 55.2 |
| End-of-Injection (° ATDC) | -201.4 | -286.4 |

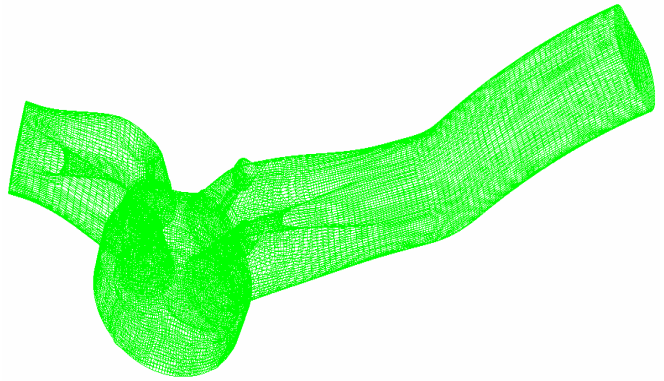

**Figure 22** Computational mesh of the Gasoline Turbocharged Direct Injection engine at -50° CA ATDC

The computational mesh contains around 190,000 cells, including the intake and exhaust manifolds and the cylinder, as can be seen in Figure 22. Figure 23 shows the overall residual mass fraction of the cylinder and the average residual of the flame front cells for the high-load, uniform-mixture case (note that the flame front is not defined before the time of ignition). Figure 24 shows the overall residual mass fraction of the cylinder and the average residual of the flame front cells for the low-load, uniform-mixture case. From Figure 23 and Figure 24 it is seen that the overall residual nearly doesn't change, but the residual in the flame front cells has some variations around the overall residual value. The changing residual value in the flame front cells affects the laminar flame speed locally.

Figures 25 (a,b) show a comparison between the species "Ar" mass fraction distributions and the total local inert species distribution for the high-load, uniform-mixture case. In Figure 25, the crank angle at the end of the compression stroke is defined as 720 degrees, and the red surface is the flame front G=0 iso-surface. From Figure 25 it is seen that the residual at the flame front cells from the transport equation residual model is around 1.7%, which is close to the overall residual of the engine at the high load operating condition, and thus the residual from the transport equation is considered as the local, instantaneous and accurate residual value, while the total local inert species value behind the flame front is about 20%, which does not correctly represent the real residual value.

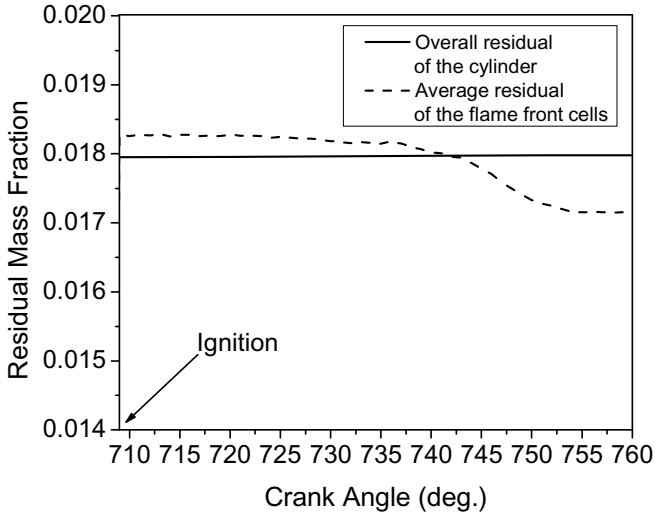


**Figure 23** Residual mass fraction of overall cylinder and flame front cells for the high load case

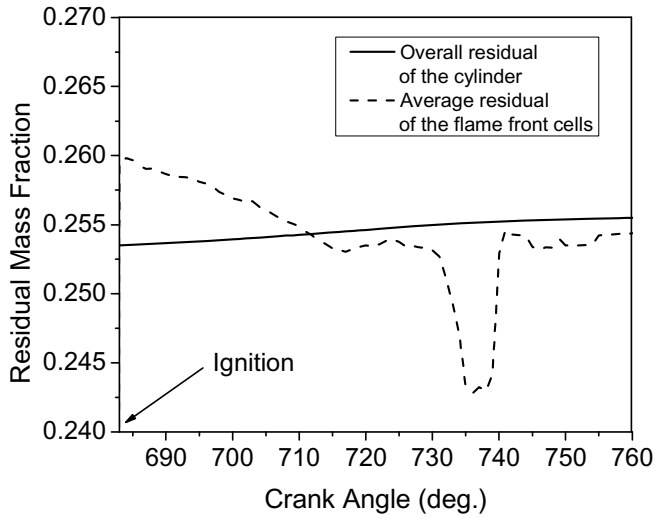


**Figure 24** Residual mass fraction of overall cylinder and flame front cells for the low load case

Figures 26 (a,b) show the corresponding comparison for the low-load, uniform-mixture case. From Figure 26 it is seen that the residual at the flame front cells from the transport equation residual model is around 25%, which is close to the overall residual. The total local inert species value at the flame front is above 30%, which does not correctly represent the real residual value.

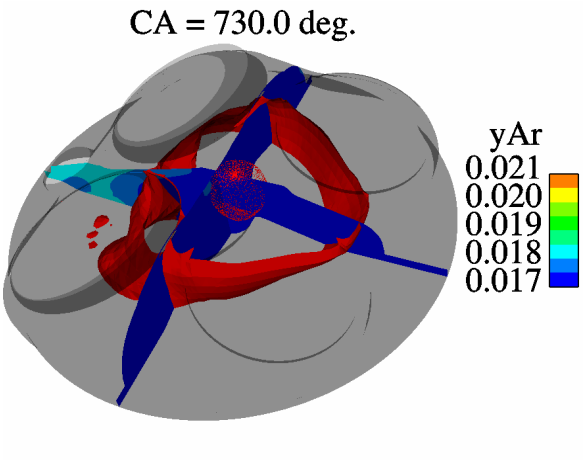


**(a)** Species “Ar” mass fraction distribution

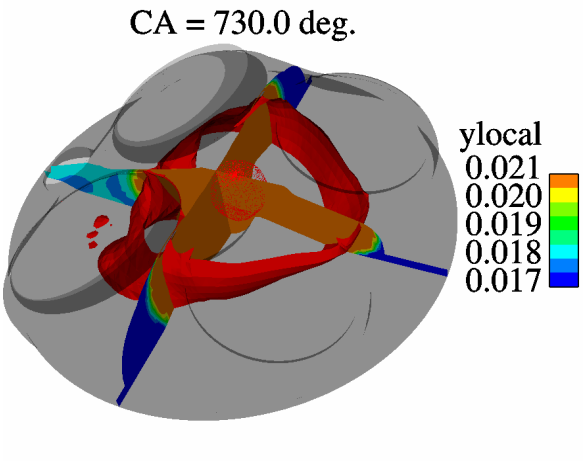


**(b)** Total local inert species distribution

**Figure 25** Comparison between species “Ar” mass fraction distribution and the total local inert species distribution for the high load case

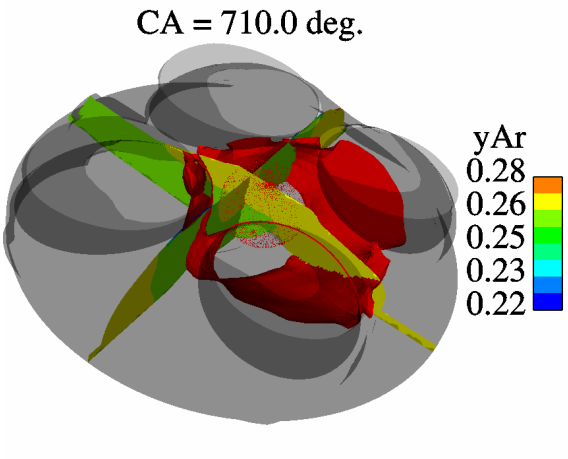


**(a)** Species “Ar” mass fraction distribution

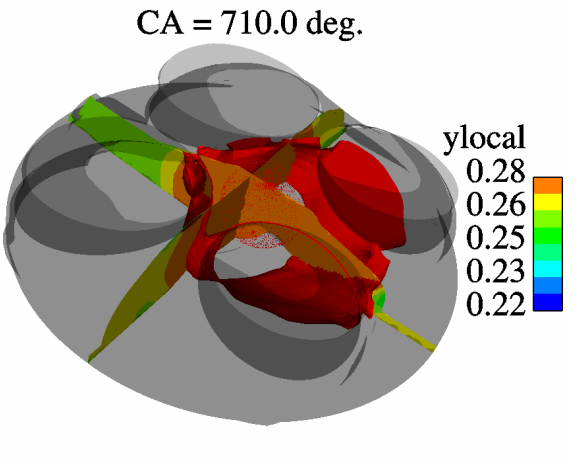


**(b)** Total local inert species distribution

**Figure 26** Comparison between species “Ar” mass fraction distribution and the total local inert species distribution for the low load case

INTEGRATED CODE USED FOR SIMULATING A GDI ENGINE

The present integrated continuous multi-component (CMC) fuel model with improved G-equation combustion and detailed chemical kinetics model was used for simulating a GDI engine. The specifications of the engine are shown in Table 5.

**Table 5** Engine specifications

| Parameters | Value |
|---|---|
| Bore (cm) | 8.9 |
| Stroke (cm) | 7.95 |
| Squish (cm) | 0.115 |
| Connecting Rod Length (cm) | 13.81 |
| Speed (rev/min) | 1500.0 |
| IVO | 10° BTDC |
| IVC | 60° ABDC |
| EVO | 12° BBDC |
| EVC | 58° ATDC |
| Spark Ignition Timing | 32° BTDC |
| Injection Timing | 78.15° BTDC |
| Injection Duration (° CA) | 6.15 |
| Injection Amount (mg) | 6.9 |

This engine is a single-cylinder engine operating in the direct-injection mode. In the simulations, the stratified-charge, lean-burn operating conditions modeled include a spark timing sweep, an EOI sweep and a MAP sweep. The global A/F ratio in the studied cases varies from 30 to 60. The internal residual levels vary from 6% to 12% according to the intake flow simulations. Simulated in-cylinder pressures and heat release rates were compared to measured data from dynamometer engine tests [27,28]. The same set of combustion model constants (cm1=2.0, cm2=0.88) were applied to all cases. The results are shown in Figures 27, 28, and 29.

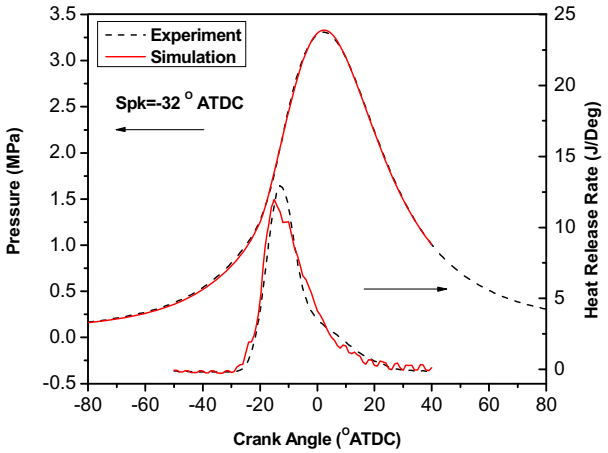


**(a)** Spark timing -32° ATDC

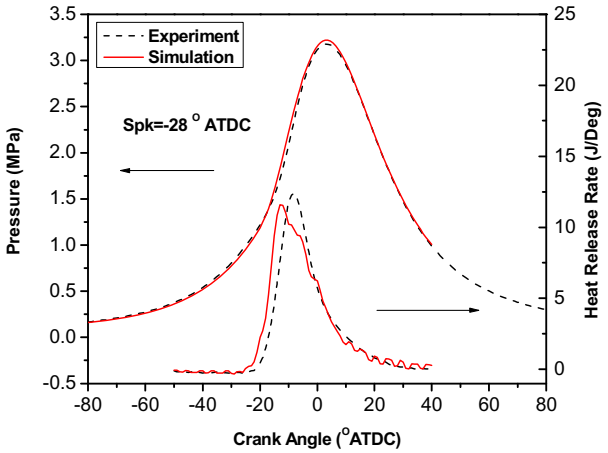


**(b)** Spark timing -28° ATDC

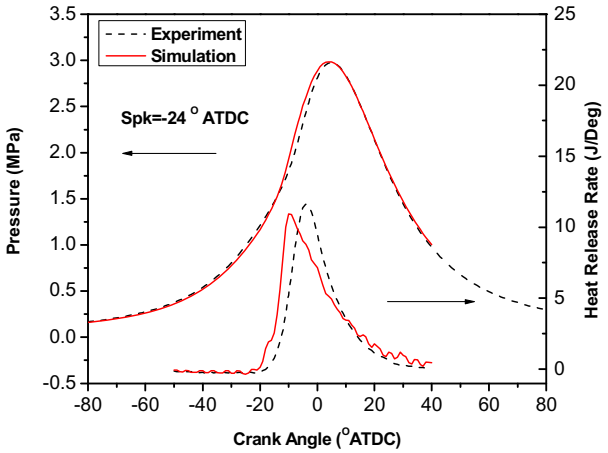


**(c)** Spark timing -24° ATDC

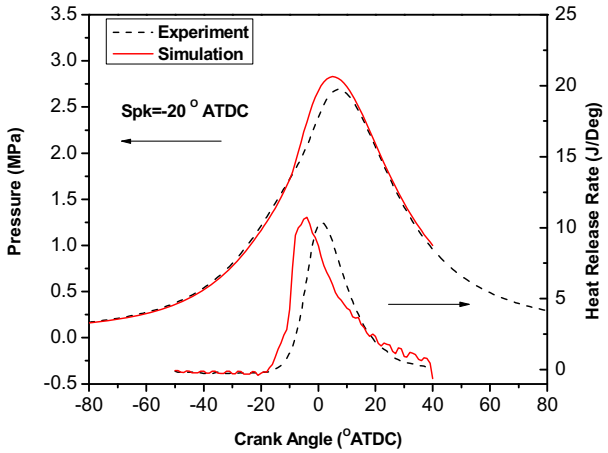


**(d)** Spark timing -20° ATDC

**Figure 27** Spark timing sweep

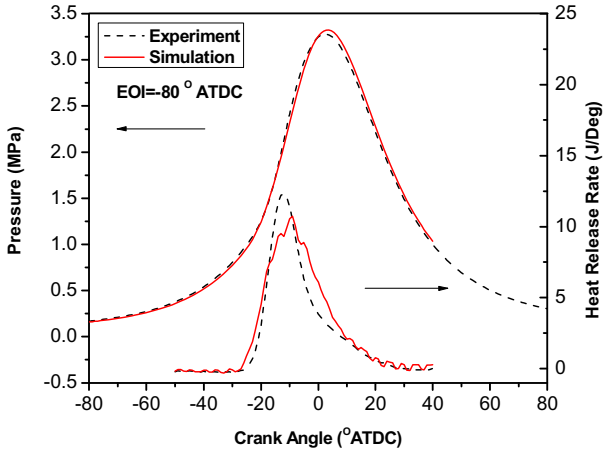


**(a)** End of injection -80° ATDC

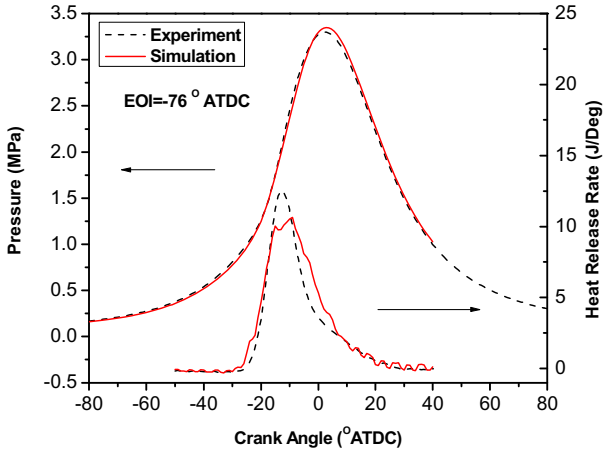


**(b)** End of injection -76° ATDC

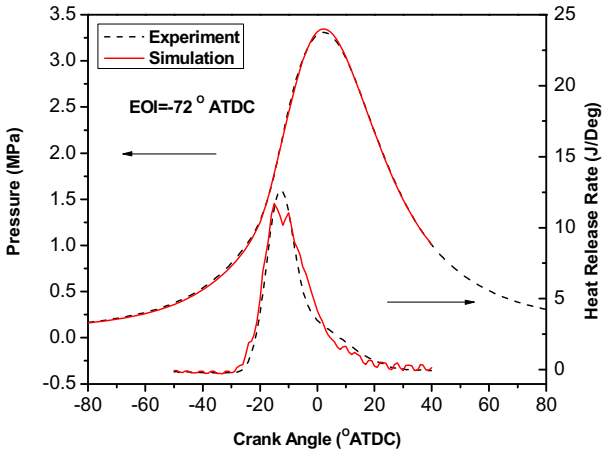


**(c)** End of injection -72° ATDC

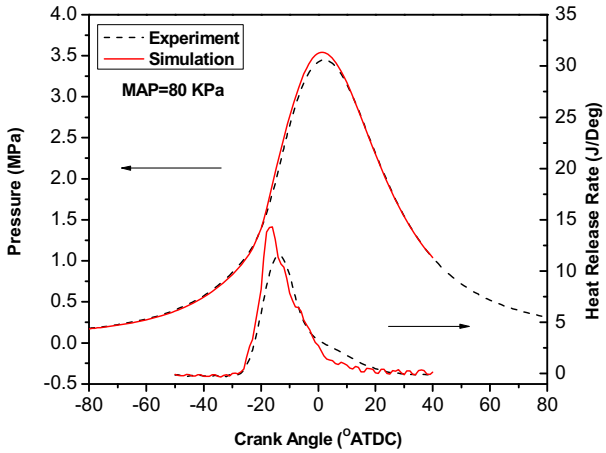


**(b)** MAP 80 kPa

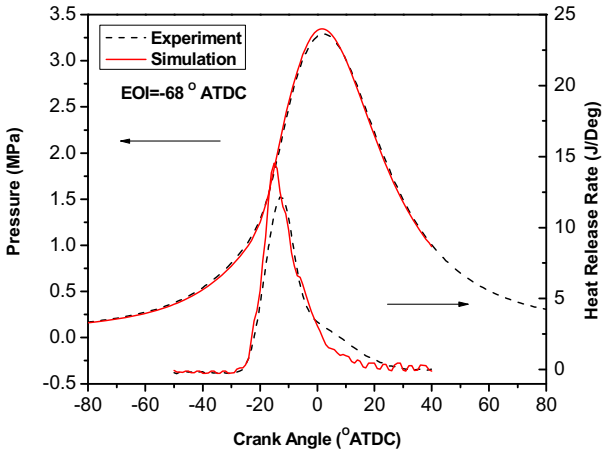


**(d)** End of injection -68° ATDC

**Figure 28** End of injection sweep

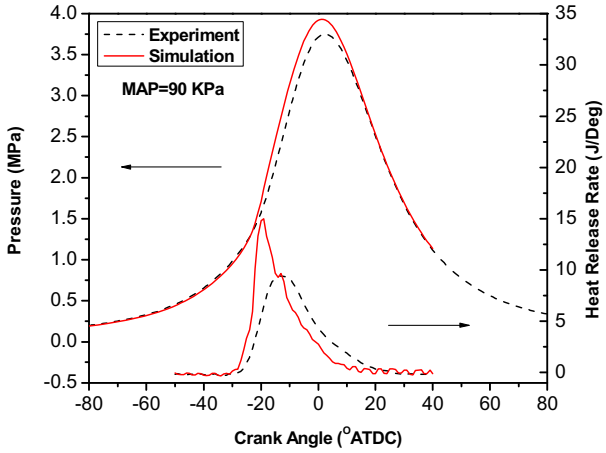


**(c)** MAP 90 kPa

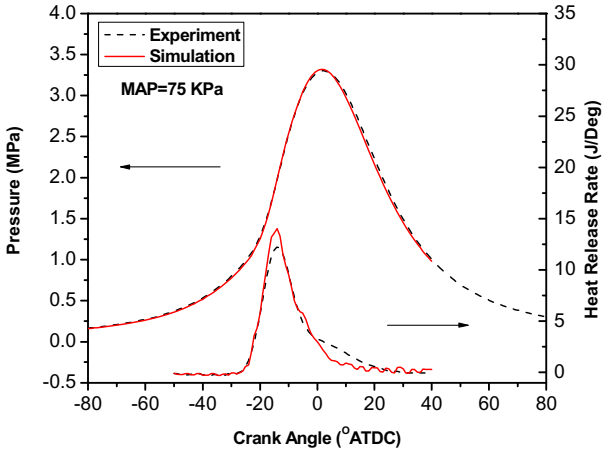


**(a)** MAP 75 kPa

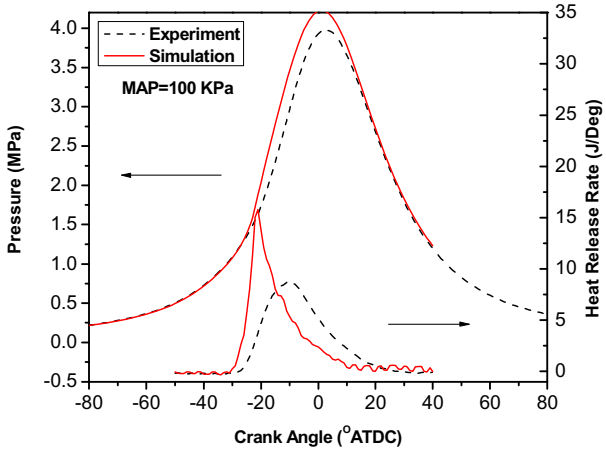


**(d)** MAP 100 kPa

**Figure 29** MAP sweep

Modeling results of the spark timing sweep cases are shown in Figure 27 and very good agreement was obtained between simulated and measured pressures and heat release rates (MAP = 75 kPa, EOI = -72° ATDC). Comparisons of simulated and measured pressures and heat release rates for the EOI sweep

cases are shown in Figure 28 (MAP = 75 kPa, spark timing = -32° ATDC). Reasonably good agreement was obtained between the simulation results and the experimental data. Both the experiment and the simulation demonstrate that the engine performance does not change significantly with slight tuning of fuel injection timing in the cases studied. Modeling results of the MAP sweep cases are shown in Figure 29 (spark timing = -32° ATDC, EOI = -68° ATDC). Although relatively larger discrepancies between computed and measured pressures and heat release rates for the MAP = 90 and 100 kPa cases are observed, good agreements are obtained between simulated and measured pressure and heat release rate for the other manifold absolute pressures.

## CONCLUSION

In this study a continuous multi-component fuel evaporation model has been integrated with an improved G-equation combustion and detailed chemical kinetics model. The integrated code has been successfully used to simulate a gasoline direct-injection engine. To consider the change of local fuel vapor mixture composition, a "PRF adaptive" method is proposed that formulates a relationship between the fuel vapor mixture PRF number (or Octane number) and the fuel vapor mixture composition based on the mean molecular weight and variance of the fuel vapor mixture composition in each cell. The laminar flame speed was updated to account for multi-component fuel effects. The updated laminar flame speed is a function of pressure, temperature, equivalence ratio, residual, and fuel vapor mixture PRF number. To model the chemistry process in the unburned region in front of the flame and in burned regions behind the flame, a recently developed PRF mechanism is used to describe the combustion process of the multi-component fuel mixture. Based on the results, the following conclusions can be drawn:

1. Multi-component fuels such as gasoline obviously have different vaporization characteristics from single component fuels such as iso-octane in that the vapor fuel distributions of their sprays are quite different. Therefore a multi-component fuel model is necessary for more accurate predictions of the fuel distribution in the engine cylinder. The present continuous multi-component (CMC) fuel model captures important multi-component fuel characteristics, and saves computing time compared with discrete multi-component (DMC) fuel models since only two additional transport equations are needed.

2. The improved G-equation combustion and detailed chemical kinetics model, which includes a transport equation residual model, a Damkohler number criterion model, and a new PRF mechanism, has higher accuracy for predicting the flame propagation, calculating the residual effect on the laminar flame speed, determining the relevant combustion regime in the flame-containing cells, and predicting the ignition delay in unburned regions of gasoline engines.

3. The proposed "PRF adaptive" method presented in this paper allows integration of the continuous multi-component (CMC) fuel model and the G-equation combustion model. Inclusion of multi-component fuel effects on the laminar flame speed is also necessary and was implemented for accurate combustion modeling.

## ACKNOWLEDGMENTS

This work was supported by Ford Research and Advanced Engineering. The authors thank Drs. Youngchul Ra and Long Liang for helpful discussions and comments. Ford Research and Advanced Engineering is thanked for providing experimental test data.

## REFERENCES

1. Amsden, A. A., Butler, T. D., O'Rourke, P. J., and Ramshaw, J. D.. KIVA–A Comprehensive Model for 2-D and 3-D Engine Simulations. SAE Paper 850554.
2. Amsden, A. A., O'Rourke, P. J., and Butler, T. D.. KIVA–II: A Computer Program for Chemically Reactive Flows with Sprays. Los Alamos National Laboratory Report, LA-11560-MS, 1989.
3. Amsden, A. A.. KIVA–3: A KIVA Program with Block-Structured Mesh for Complex Geometries. Los Alamos National Laboratory Report, LA-12503-MS, 1993.
4. Amsden, A. A.. KIVA–3V: A Block-Structured KIVA Program for Engines with Vertical or Canted Valves. Los Alamos National Laboratory Report, LA-13313-MS, 1997.
5. Amsden, A. A.. KIVA–3V, Release 2, Improvements to KIVA–3V. Los Alamos National Laboratory Report, LA-13608-MS, 1999.
6. Lippert, A. M.. Modeling of Multi-Component Fuels with Application to Sprays and Simulation of Diesel Engine Cold Start. Ph.D. Thesis, University of Wisconsin-Madison, 1999.
7. Zhu, G.-S. and Reitz, R. D.. A Model for High Pressure Vaporization of Droplets of Complex Liquid Mixtures Using Continuous Thermodynamics. Int. J. Heat Mass Transfer, 45: 495-507, 2002.
8. Tamim, J. and Hallett, W. L. H.. Continuous Thermodynamics Model for Multi-Component Vaporization. Chem. Engr Sci., 50(18): 2933-2942, 1995.
9. Lippert, A. M. and Reitz, R. D.. Modeling of Multi-Component Fuels Using Continuous Distributions with Application to Droplet Evaporation and Sprays. SAE Paper 972882, 1997.
10. Zuo, B. F., Gomes, A. M., and Rutland, C. J.. Modeling of Superheated Fuel Spray and Vaporization. Int. J. Engine Res., 1(4): 321-336, 2000.

11. Davy, M. H., Williams, P. A., and Anderson, R. W.. Effects of Fuel Composition on Mixture Formation in a Firing Direct-Injection Spark-Ignition (DISI) Engine: An Experimental Study Using Mie-Scattering and Planar Laser-Induced Fluorescence (PLIF) Techniques. SAE Paper 2000-01-1904, 2000.
12. Ra, Y. and Reitz, R. D.. The Application of a Multi-Component Droplet Vaporization Model to Gasoline Direct Injection Engines. Int. J. Engine Res., 4(3): 193-218, 2003.
13. Heywood, J. B.. Internal Combustion Engine Fundamentals. McGraw-Hill, 1988.
14. Peters, N.. Turbulent Combustion. Cambridge University Press, Cambridge, UK, 2000.
15. Fan, L. and Reitz, R. D.. Development of Ignition and Combustion Model for Spark-Ignition Engines. SAE Paper 2000-01-2809, 2000.
16. Williams, F. A.. Turbulent Combustion. SIAM, Philadelphia, 1985.
17. Peters, N.. The Turbulent Burning Velocity for Large Scale and Small Scale Turbulence. J. Fluid Mech., 384: 107-132, 1999.
18. Dekena, M. and Peters, N.. Combustion Modeling with the G-equation. Oil & Gas Science and Technology-Rev. IFP, 54(2): 265-270, 1999.
19. Tan, Z.. Multi-Dimensional Modeling of Ignition and Combustion in Premixed and DIS/CI (Direct Injection Spark/Compression Ignition) Engines. Ph.D. Thesis, University of Wisconsin-Madison, 2003.
20. Ewald, J. and Peters, N.. A Level Set Based Flamelet Model for the Prediction of Combustion in Spark Ignition Engines. 15th International Multidimensional Engine Modeling User's Group Meeting, Detroit, MI, 2005.
21. Curran, H. J., Gaffuri, P., Pitz, W. J., and Westbrook, C. K.. A Comprehensive Modeling Study of Iso-octane Oxidation. Combustion and Flame, 129(3): 253-280, 2002.
22. Liang, L. and Reitz, R. D.. Spark Ignition Engine Combustion Modeling Using a Level Set Method with Detailed Chemistry. SAE Paper 2006-01-0243, 2006.
23. Liang, L., Reitz, R. D., Iyer, C. O., and Yi, J.. Modeling Knock in Spark-Ignition Engines Using a *G*-equation Combustion Model Incorporating Detailed Chemical Kinetics. SAE Paper 2007-01-0165, 2007.
24. Liang, L.. Multidimensional Modeling of Combustion and Knock in Spark-Ignition Engines with Detailed Chemical Kinetics. Ph.D. Thesis, University of Wisconsin-Madison, 2006.
25. Tan, Z., Kong, S. C., and Reitz, R. D.. Modeling Premixed and Direct Injection SI Engine Combustion Using the G-Equation Model. JSAE/SAE International Spring Fuels & Lubricants Meeting, Japan, JSAE Paper 2003-01-1843, 2003.
26. Tan, Z. and Reitz, R. D.. Modeling Ignition and Combustion in Spark-Ignition Engines Using a Level Set Method. SAE Paper 2003-01-0722, 2003.
27. Yang, S., Reitz, R. D., Iyer, C. O., and Yi, J.. Improvements to Combustion Models for Modeling Spark-Ignition Engines Using the G-equation and Detailed Chemical Kinetics. SAE Paper 2008-01-1634, 2008.
28. Yang, S., Reitz, R. D., Iyer, C. O., and Yi, J.. A Transport Equation Residual Model Incorporating Refined G-Equation and Detailed Chemical Kinetics Combustion Models. SAE Paper 2008-01-2391, 2008.
29. Chou, G. F. and Prausnitz, J. M.. Adiabatic Flash Calculations for Continuous or Semi-Continuous Mixtures Using an Equation of State. Fluid Phase Equilibria, 30: 75-82, 1986.
30. Han, Z. and Reitz, R. D.. Turbulence Modeling of Internal Combustion Engines Using RNG $\kappa$-$\varepsilon$ Models. Comb. Sci. Tech., 106:267–295, 1995.
31. Metghalchi, M. and Keck, J. C.. Burning Velocities of Mixtures of Air with Methanol, Isooctane, and Indolene at High Pressure and Temperature. Combustion and Flame, 48:191–210, 1982.
32. Zhao, Z., Conley, J. P., Kazakov, A., and Dryer, F. L.. Burning Velocities of Real Gasoline Fuel at 353 K and 500 K. SAE Paper 2003-01-3265, 2003.
33. Tamagna, Daniele, Gentili, Roberto, Ra, Youngchul, and Reitz, R. D.. Multidimentional Simulation of the Influence of Fuel Mixture Composition and Injection Timing in Gasoline-Diesel Dual-Fuel Applications. SAE Paper 2008-01-0031, 2008.
34. Rose, J. W. and Cooper, J. R.. Technical Data on Fuel. New York: Wiley, 1977.
35. Kalghatgi, Gautam T.. Auto-Ignition Quality of Practical Fuels and Implications for Fuel Requirements of Future SI and HCCI Engines. SAE Paper 2005-01-0239, 2005.
36. Huang, Y., Sung, C. J., and Eng, J. A.. Laminar Flame Speeds of Primary Reference Fuels and Reformer Gas Mixtures. Combustion and Flame, 139: 239-251, 2004.
37. Ryan, T. W. and Lestz, S. S.. The Laminar Burning Velocity of Iso-octane, n-heptane, Methanol, Methane, and Propane at Elevated Temperature and Pressure in the Presence of a Diluent. SAE Paper 800103, 1980.
38. Kong, S.-C., Marriott, C. D., Reitz, R. D., and Christensen, M.. Modeling and Experiments of HCCI Engine Combustion Using Detailed Chemical Kinetics with Multidimensional CFD. SAE Paper 2001-01-1026, 2001.
39. Kong, S.-C. and Reitz, R. D.. Application of Detailed Chemistry and CFD for Predicting Direct Injection HCCI Engine Combustion and Emissions. Proc. Combust. Inst., 29:663–669, 2002.
40. Kee, R. J., Rupley, F. M., and Miller, J. A.. CHEMKIN-II: A FORTRAN Chemical Kinetics Package for the Analyses of Gas Phase Chemical Kinetics. Technical report, Sandia Report, 1989.
41. Tanaka, S., Ayala, F., and Keck, J. C.. A Reduced Chemical Kinetic Model for HCCI Combustion of

Primary Reference Fuels in a Rapid Compression Machine. Combustion and Flame, 133:467–481, 2003.
42. Fieweger, K., Blumenthal, R., and Adomeit, G.. Self-Ignition of S.I. Engine Model Fuels: A Shock Tube Investigation at High Pressure. Combustion and Flame, 109:599–619, 1997.
43. Ra, Y. and Reitz, R. D.. A Reduced Chemical Kinetic Model for IC Engine Combustion Simulations with Primary Reference Fuels. Combustion and Flame (2008), doi:10.1016/j.combustflame.2008.05.002.
44. Tan, Z. and Reitz, R. D.. An Ignition and Combustion Model Based on the Level-Set Method for Spark Ignition Engine Multi-Dimensional Modeling. Combustion and Flame, 145:1–15, 2006.

## CONTACT

Shiyou Yang
Engine Research Center
University of Wisconsin-Madison
1500 Engineering Drive, Madison, WI 53706, USA
yang29@wisc.edu 1-608-265-8608

## ABBREVIATIONS

**GDI**: gasoline direct injection
**PRF**: primary reference fuel
**DMC**: discrete multi-component
**CMC**: continuous multi-component
**SI**: spark ignition
**DPIK**: discrete particle ignition kernel
**PDF**: probability density function
**GTDI**: gasoline turbocharged direct injection
**EGR**: exhaust gas recirculation
**CN**: cetane number
**MW**: molecular weight
**RON**: research octane number
**WSR**: well stirred reactor
**HCCI**: homogeneous charge compression ignition
**RCM**: rapid compression machine
**CA**: crank angle
**SMD**: sauter mean diameter
**IVO**: intake valve open
**IVC**: intake valve close
**EVO**: exhaust valve open
**EVC**: exhaust valve close
**ATDC**: after top dead center
**BTDC**: before top dead center
**ABDC**: after bottom dead center
**BBDC**: before bottom dead center
**MAP**: manifold absolute pressure
**EOI**: end of injection
**ON**: octane number
**DI**: direct injection
**CFD**: computational fluid dynamics